How high frequency atmospheric forcing impacts mesoscale eddy surface signature and vertical structure

Alexandre Barboni[1], alexandre stegner[2], Franck DUMAS[3], and Xavier J. Carton[4]

[1]École Polytechnique
[2]Laboratoire de Météorologie Dynamique, CNRS, IPSL
[3]SHOM
[4]Universite de Bretagne Occidentale

December 14, 2023

How atmospheric forcing frequency, horizontal and vertical grid resolutions impact mesoscale eddy evolution in a numerical model

Alexandre Barboni [1,2,3], Alexandre Stegner [1], Franck Dumas [2,3], Xavier Carton [3]

[1]Laboratoire de Météorologie Dynamique/IPSL, Ecole Polytechnique, Institut Polytechnique de Paris, ENS, Université PSL, Sorbonne Université, CNRS, 91128 Palaiseau, France
[2]Service Hydrographique et Océanographique de la Marine, 29200 Brest, France
[3]Laboratoire d'Océanographie Physique et Spatiale, UBO, CNRS, IRD, Ifremer, 29280 Plouzané, France

Key Points:

- Enhanced mixing in anticyclones explains inverse eddy SST signature
- Vertical resolution is crucial to model eddy core mixing triggered by near-inertial waves
- Mixed layer anomaly is mainly driven by SST retroaction on air-sea fluxes

Corresponding author: Alexandre Barboni, alexandre.barboni@laposte.net

Abstract

Seasonal evolution of both surface signature and subsurface structure of a Mediterranean mesoscale anticyclones is assessed using the CROCO high-resolution numerical model with realistic background stratification and fluxes. In good agreement with remote-sensing and in-situ observations, our numerical simulations capture the seasonal cycle of the anomalies induced by the anticyclone, both in the sea surface temperature (SST) and in the mixed layer depth (MLD). The eddy signature on the SST shifts from warm-core in winter to cold-core in summer, while the MLD deepens significantly in the core of the anticyclone in late winter. Our sensitivity analysis shows that the eddy SST anomaly can be accurately reproduced only if the vertical resolution is high enough ($\sim 4m$ in near surface) and if the atmospheric forcing contains high-frequency. In summer with this configuration, the vertical mixing parameterized by the $k{-}\epsilon$ closure scheme is three times higher inside the eddy than outside the eddy, and leads to an anticyclonic cold core SST anomaly. This differential mixing is explained by near-inertial waves, triggered by the high-frequency atmospheric forcing. Near-inertial waves propagate more energy inside the eddy because of the lower effective Coriolis parameter in the anticyclone core. On the other hand, eddy MLD anomaly appears more sensitive to horizontal resolution, and requires SST retroaction on air-sea fluxes. These results detail the need of high frequency forcing, high vertical and horizontal resolutions to accurately reproduce the evolution of a mesoscale eddy.

Plain Language Summary

Mesoscale eddies are turbulent structures present in every regions of the world ocean, and accounting for a significant part of its kinetic energy budget. These structures can be tracked in time and recently revealed a seasonal cycle from in situ data. An anticyclone (clockwise rotating eddy in the northern hemisphere) is observed in the Mediterranean to be predominantly warm at the surface and to deepen the mixed layer in winter, but shifts to a cold-core summer signature. This seasonal signal is not yet understood and studied in ocean models. In this study we assess the realism of an anticyclone seasonal evolution in high resolution numerical simulations. Eddy surface temperature seasonal shift is retrieved and is linked to an increased mixing at the eddy core spontaneously appearing at high vertical resolution (vertical grid size smaller than 4m) in the presence of high frequency atmospheric forcing. This increased mixed is due to the preferred propagation of near-inertial waves in the anticyclone due to its negative relative vorticity. Eddy-induced mixed layer depth anomalies also appear to be triggered by sea surface temperature retroaction on air-sea fluxes. These results suggest that present-day operational ocean forecast models are too coarse to accurately retrieve mesoscale evolution.

1 Introduction

Mesoscale eddies are ubiquitous turbulent structures in the oceans, in thermal wind balance with a signature in density : positive density anomaly for an anticyclone, respectively negative for a cyclone. Eddies statistical descriptions really began with the availability of eddy automated detections based on gridded altimetry products (Doglioli et al., 2007; Chaigneau et al., 2009; Nencioli et al., 2010; Chelton, Schlax, & Samelson, 2011; Mason et al., 2014; Le Vu et al., 2018; Laxenaire et al., 2018). The first quantitative studies were done in a composite approach : many daily snapshots detections are colocated with eddy contours and gathered into a single annual mean eddy signature (Hausmann & Czaja, 2012; Everett et al., 2012). This approach combined with remote-sensing measurements provides an extensive view of eddies in various regions of the global ocean, with SST, sea surface salinity (Trott et al., 2019), chlorophyll (Chelton, Gaube, et al., 2011) and also meteorological variables (Frenger et al., 2013). Composite approach also allowed to reveal a modulation of air-sea fluxes at the eddy scale : in the Agulhas retroflexion region, (Villas Bôas et al., 2015) showed the total heat flux to the atmosphere to be enhanced over very strong and warm anticyclones. Similarly for the eddy vertical structure, gathering Argo profiles as a function of normalized distance to the eddy center, eddies were found to influence the mixed layer depth (MLD) (Sun et al., 2017; Gaube et al., 2019). Anticyclones have deeper MLD in their core, cyclones shallower MLD, with larger mixed layer anomalies in winter. Eddies were also observed to incorporate a significant seasonal cycle in their radius variations (Zhai et al., 2008) and their SST signature (Sun et al., 2019; Y. Liu et al., 2021). Anticyclones (respectively cyclones) usually identified as warm in surface, actually shift to cold (warm) signatures in summer in several regions of the world ocean (Sun et al., 2019; Moschos et al., 2022). This phenomenon is then referred to as 'inverse' SST signatures. (Moschos et al., 2022) showed that these 'inverse' signatures actually become predominant in summer in the Mediterranean Sea, a seasonal shift yet not properly understood.

The composite approach is nonetheless ill-suited to study eddy temporal variability due to the stacking of numerous observations in time. Recently Lagrangian approaches were developed to study eddies enabling to better track their temporal variability (Pessini et al., 2018; Laxenaire et al., 2020; Barboni et al., 2021). Using a Lagrangian approach, Moschos et al. (2022) showed that the same individual anticyclones shift from a warm winter SST anomaly to a cold one in summer (and conversely for cyclone). With the additional Argo floats trapped in anticyclones, they further noticed that anticyclonic density anomaly remains warmer at depth while becoming colder in surface, leading to a smoother density gradient. Hence the hypothesis that this seasonal shift could be explained by a modulation of the vertical mixing by mesoscale eddies, anticyclones (cyclones) likely enhancing (decreasing) mixing in surface. Recent observations in the Mediterranean Sea of inside-anticyclone properties temporal evolution further revealed eddy mixed layer anomalies to be much larger than the composite approach mean value, reaching sometimes 300m (Barboni, Coadou-Chaventon, et al., 2023). MLD anomalies evolution was also shown to have evolution much faster than the month, with delayed restratification inside anticyclones. Mechanisms driving these MLD anomalies are also unexplained, but Barboni, Coadou-Chaventon, et al. (2023) found it to be impacted by interactions with the anticyclone vertical structure.

An eddy modulation of vertical mixing was recently investigated to be linked with a modulation of near-inertial waves (NIW) propagation. NIW can not propagate at frequencies lower than the inertial frequency f due to Earth rotation (Garrett & Munk, 1972). However in the presence of a balanced flow, anticyclones (cyclones) with negative (positive) relative vorticity ζ locally shift this cut-off to an effective inertial frequency $f_e = f + \zeta/2$ (Kunze, 1985). Sub-inertial waves ($\omega \lesssim f$) can then remained trapped in anticyclones and supra-inertial waves ($\omega \gtrsim f$) can be expelled from cyclones. Consequently, NIW propagate more inside anticyclones, what was experimentally (D'Asaro, 1995) and numerically (Danioux et al., 2008, 2015; Asselin & Young, 2020) proven. This NIW trapping potential partly explains the interest in anticyclones rather than in cyclones, the other reason likely being that anticyclones are more stable in time (Arai & Yamagata, 1994; Graves et al., 2006), in particular for large structures (Perret et al., 2006), then more easily detected and trapping more often profilers (thus easing field campaigns). Several recent observations (Martínez-Marrero et al., 2019; Fernández-Castro et al., 2020) showed that mixing at depth is enhanced below anticyclones due to this more energetic NIW propagation. On the other hand numerical studies assumed extremely simplified set-up with constant wind (Danioux et al., 2008) or an idealized wind burst (Asselin & Young, 2020). They also looked at NIW propagation in an eddying field at short time scales, then without significant evolution of the eddies and stratification. Eddy-NIW interaction on longer time scales - eddy evolving time scales like months - in a varying stratification due to seasonal cycle has never been assessed so far. In particular the effect of this differential NIW propagation on eddies remains unknown and a gap remains to link wave propagation and enhanced mixing.

Some recent studies started to assess eddy temporal evolution in high resolution regional models. In the Mediterranean Sea, Escudier et al. (2016) compared eddy size, drift and lifetime compared to eddies in altimetric observations. Mason et al. (2019) investigated these variables in assimilated operational models and additionally looked at MLD anomalies, but both were in a composite approach and did not look at eddy SST variations. More recently Stegner et al. (2021) performed an observation system simulation experiment on a 1/60°simulation of the Mediterranean sea and found great bias on size and strength for small eddy detections, but did not look at SST variations. Using the same simulation, an interesting method was developed by Ioannou et al. (2021), investigating differences in both trajectories, size and stratification of the Ierapetra anticyclonic eddy, but restricted to this particular case.

Eddy SST anomalies seasonal shift and mixed layer depth anomalies remain poorly investigated so far in ocean models. If NIW propagation and eddy vertical structure are considered, grid resolution - both horizontal and vertical - and atmospheric forcing are likely key aspects to take into account. Air-sea fluxes and near-inertia-gravity waves involve much shorter temporal and spatial scales, not reproduced even in eddy-permitting models at present stage. We then aim to assess the realism of an anticyclone seasonal signal, in both surface and mixed layer, using an idealized but high-resolution simulation and investigating driving physical processes. The goal is to assess the realism of the eddy temporal evolution compared to similar observations, in particular the retrieval of the surface signature seasonal cycle. In a first part we conduct a sensitivity analysis on horizontal grid cell. In a second part we study the sensitivity to atmospheric forcing frequency. Last, the effect of SST retroaction on air-sea fluxes is discussed.

2 Methods

2.1 Model set-up

Idealized numerical experiments are performed using the Coastal and Regional Ocean Community (CROCO) model. CROCO is based on the Regional Ocean Modeling System (ROMS) kernel (Shchepetkin & McWilliams, 2005). It uses a time splitting method between the fast barotropic mode and the slow baroclinic ones. Advection schemes are UP3 for horizontal and Akima-Splines for the vertical. Trying to conciliate realistic and idealized approach, we use double periodic conditions in a realistic stratification and on long timescale. The atmospheric forcing has realistic temporal variations but is spatially homogeneous. The only active tracer used is temperature. As a consequence, a linear state equation links density ρ and temperature T, with thermal expansion $T_c = 0.28 kg.m^{-3}.K^{-1}$ and linear approximation close to $T_0 = 25$°C and $\rho_0 = 1026 kg.m^{-3}$:

$$\rho = \rho_0 + T_c(T - T_0) \tag{1}$$

Discarding salinity effects is justified by the very weak salinity seasonal cycle in the Mediterranean Sea. The heat flux seasonal cycle is roughly $\pm 150\, W.m^{-2}$ (Pettenuzzo et al., 2010), whereas salinity fluxes are mostly driven by the evaporation minus precipitation balance, with a mean of roughly $10^3 mm/y$, a seasonal cycle maximal amplitude of $\Delta F = 4 \times 10^2 mm/y$ and river input being negligible (Mariotti, 2010). Considering a haline contraction coefficient of $S_c = 0.78 kg.m^{-3}.PSU^{-1}$, a ΔF freshwater input would have a seasonal equivalent effect on buoyancy $Q_{eq} = \rho_0 c_p \frac{S_c}{T_c} S_0 \Delta F \approx 5\, W.m^{-2}$, indeed almost two orders of magnitude lower than Q_{tot}.

Grid

Simulation domain is double periodic, on the f-plane, with a flat bottom $H_{bot} = 3000m$. Horizontal extent is 200km in both directions, with horizontal resolution ranging between 4km and 500m, with 25 to 150 vertical levels. Coriolis parameter is $f = 9.0\times10^{-5}s^{-1}$. CROCO uses a σ terrain-following coordinate, the N vertical levels being modulated in time between bottom and sea surface height η. Constant depth level z_0 are stretched over thickness h_c with surface coefficient θ_s :

$$z = \eta + (\eta + H_{bot})z_0 \tag{2}$$

$$z_0 = \frac{h_c\sigma + H_{bot}C_s(\sigma)}{h_c + H_{bot}} \quad \text{with} \quad C_s(\sigma) = \frac{1 - cosh\left(\theta_s \frac{\sigma - N}{N}\right)}{cosh(\theta_s) - 1} \tag{3}$$

With $N = 100$ levels, $h_c = 400m$ and $\theta_s = 8$, vertical grid step dz is then $3.5m$ in the upper $200m$. $200m$ being the vertical scale of the thermocline, it ensures a maximal resolution in the upper ocean where seasonal variations occur (Houpert et al., 2015). This configuration has then a higher vertical resolution than previous similar studies ($N = 32$, $h_c = 250m$ and $\theta_s = 6.5$ for Escudier et al. (2016)) or operational models (Juza et al., 2016).

Turbulent closure

Mixing is parameterized through $k{-}\epsilon$ closure scheme (Rodi, 1987) using the generic length scale approach (Umlauf & Burchard, 2003). Turbulent kinetic energy k dissipates with rate ϵ and stability function c_v into an effective viscosity ν (respectively c_T and κ for diffusivity). No additional explicit mixing is added.

$$\nu = \frac{c_v k^2}{\epsilon} \quad \text{and} \quad \kappa = \frac{c_T k^2}{\epsilon} \tag{4}$$

A minimal k input is parameterized. Given that the minimal dissipation rate ϵ is set to $10^{-12}W.kg^{-1}$, the minimal k has to be set to $10^{-9}m^2.s^{-2}$ in order to retrieve a minimal diffusivity of $10^{-6}m^2.s^{-1}$ with a stability function of order unity. This diffusivity value is close to kinematic viscosity and thermal diffusivity for water (respectively 1×10^{-6} and $1\times10^{-7}\,m^2.s^{-1}$). This issue was also discussed by Perfect et al. (2020).

2.2 Background stratification and initial mesoscale anticyclone

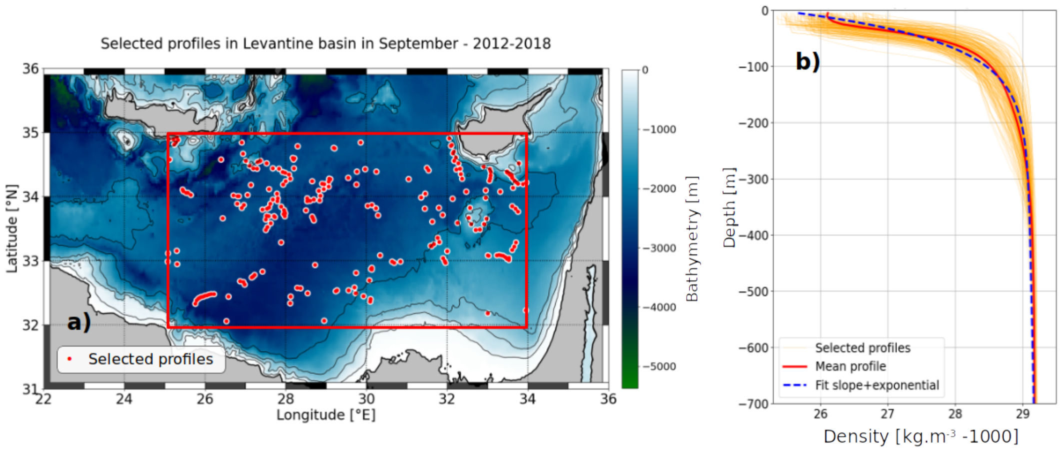

Figure 1. (a) Map showing the region of high long-lived anticyclones occurrence in the Levantine basin. The atmospheric fields used as input are averaged over the area delimited by the red frame. Red dots are the cast position of 242 selected in situ profiles identified as outside-eddy. Bathymetry is ETOPO1 data (Smith & Sandwell, 1997) with 0, 500, 1000 and 1500m isobaths. (b) Selected density profiles (orange thin lines), mean profile (red thick line) and fitted profile using Eq.5 (blue dashed).

A realistic background stratification is set from a climatological database gathering in situ data from Copernicus Marine Environment Monitoring Service (Barboni, Stegner, et al., 2023). A region of interest is considered at the center of the Levantine Basin (25 to 34 °E and 32 to 35 °N, shown in Fig.1a). For background stratification we used only profiles in the region of interest, detected as outside-eddy using the DYNED eddy atlas dataset (see Barboni, Coadou-Chaventon, et al. (2023) for details), from 2012 to 2018 and for each year in September. Considering these criteria, 242 profiles are averaged into a mean stratification $\rho_b(z)$ fitted over the first 1000m with a linear slope S added to an upper ocean thermocline with exponential shape and vertical scale Z_T (Eq.5, see Fig.1b). September is chosen as the end of summer when the thermocline is marked and stratification gradient the strongest, allowing a better fit with exponential slope.

$$\rho_b(z) = \rho_1 + (\rho_s - \rho_1) exp\left(-\frac{z}{Z_T}\right) + Sz \tag{5}$$

Regression fit gave $\rho_1 = 1029.03 kg.m^{-3}$, $\rho_s = 1025.3 kg.m^{-3}$, $Z_T = 55m$, $S = 1.8 \times 10^{-4} kg.m^{-4}$. Corresponding baroclinic deformation radius R_d is approximately $11km$. An initial density anomaly σ in geostrophic equilibrium is added to the background stratification. $\sigma(r,z)$ is azimuthally symmetric and has a Gaussian shape in the vertical direction and pseudo-Gaussian in the radial one, with radius R_{max} and vertical extent H :

$$\sigma(r,z) = \sigma_0 \frac{z}{H} exp\left(-\frac{1}{\alpha}\left(\frac{r}{R_{max}}\right)^{\alpha}\right) exp\left(-\frac{1}{2}\left(\frac{z}{H}\right)^2\right) \quad \text{with} \quad \sigma_0 = \frac{\rho_0 f V_{max} R_{max} e^{1/\alpha}}{gH} \tag{6}$$

The initial maximal speed radius R_{max} is 25 km, slightly more than twice the deformation radius but still smaller than the large long-lived Eastern Mediterranean anticyclones (Barboni, Coadou-Chaventon, et al., 2023), giving a Burger number ($Bu = R_d^2/R_{max}^2$) close to 0.2. Maximal speed is initially set to $V_{max} = 0.4\, m.s^{-1}$ giving a Rossby number ($Ro = V_{max}/R_{max}f$) of 0.16, but later decays around 0.1. $Ro = 0.1$ is a standard value in the Mediterranean Sea (Ioannou et al., 2019). H is set to $100m$ on the same order as thermocline extent Z_T, and shape parameter $\alpha = 1.6$ ensures barotropic stability (Carton et al., 1989; Stegner & Dritschel, 2000). Cyclogeostrophic correction is added following Penven et al. (2014).

2.3 Atmospheric heat forcing

ERA5 reanalysis input is used for atmospheric forcing. Fields are available with a 1 hour temporal resolution and 1/4°horizontal resolution (Hersbach et al., 2020). Retrieved variables are surface short wave Q_{SW}^{surf}, downward long wave flux $Q_{LW}^{\downarrow}$, sea level pressure P_{SL}, h_{2m} and T_{2m} relative humidity and temperature at 2m above surface, and last u and v 10m neutral zonal and meridional wind components. To focus on the temporal variability, these time series are spatially averaged over the Levantine basin (Fig.1a). Air-sea fluxes are then computed with the Coupled Ocean–Atmosphere Response Experiment (COARE) 3.0 parametrization (Fairall et al., 2003), with improved accuracy for large wind speeds ($> 10m.s^{-1}$) encountered in high frequency forcing. Net heat flux Q_{tot} is defined as the sum of surface short wave, long wave (upward $Q_{LW}^{\uparrow}$ and downward $Q_{LW}^{\downarrow}$ components), latent (Q_{Lat}) and sensible (Q_{Sen}) fluxes, convention positive fluxes downwards :

$$Q_{tot} = Q_{SW}^{surf} + Q_{LW}^{\uparrow} + Q_{LW}^{\downarrow} + Q_{Lat} + Q_{Sen} \tag{7}$$

$Q_{tot} - Q_{SW}^{surf}$ is applied directly at the surface, while short wave heat flux $Q_{SW}(z)$ is distributed on the vertical following Paulson and Simpson (1977) transparency model with Jerlov water type I , consistent with very clear Mediterranean waters ($R = 0.58$, $\zeta_1 = 0.35m$, $\zeta_2 = 23m$):

$$Q_{SW}(z) = Q_{SW}^{surf}\left(Rexp\left(-\frac{z}{\zeta_1}\right) + (1-R)exp\left(-\frac{z}{\zeta_2}\right)\right) \tag{8}$$

Upward long-wave heat flux $Q_{LW}^{\uparrow}$ computes the ocean SST (T_s) thermal loss using Stefan-Boltzmann black body law, with emissivity $\epsilon_{sb} = 98.5\%$ and $\sigma_{sb} = 5.6697 \times 10^{-8}\, W.m^{-2}.K^{-4}$:

$$Q_{LW}^{\uparrow} = -\epsilon_{sb}\sigma_{sb}T_s^4 \tag{9}$$

Latent heat flux Q_{Lat} and sensible heat flux Q_{Sen} also involves a direct SST retroaction:

$$Q_{Lat} = -\rho_a L_E C_E |V|(q_s - q_a) \quad ; \quad Q_{Sen} = -\rho_a c_p C_S |V|(T_s - T_{2m}) \tag{10}$$

With ρ_a air density, c_p air thermal capacity, L_E evaporation enthalpy, $|V|$ 10m wind speed. q_s and q_a are specific humidity for ocean and atmosphere at 2m respectively. q_s is saturated at T_s and P_{SL} : $q_s = 0.98 \times 0.622 \times P_{sat}(T_s)/P_{SL}$. Factor 0.98 accounts for water vapor reduction caused by salinity (Sverdrup et al., 1942). q_a is related to saturated water pressure P_{sat} : $q_a = 0.622h_{2m}P_{sat}(T_{2m})/P_{SL}$. Last, wind stress is computed from u and v) :

$$\tau_x = \frac{\rho_a}{\rho_0} C_D |u| u \quad \text{and} \quad \tau_y = \frac{\rho_a}{\rho_0} C_D |v| v \tag{11}$$

In equations 10-11, C_E, C_S and C_D are corresponding transfer coefficients considering the stability of the atmospheric boundary layer based on the Monin-Obukhov similarity theory. They are all on the order of 1×10^{-3} (Fairall et al., 2003).

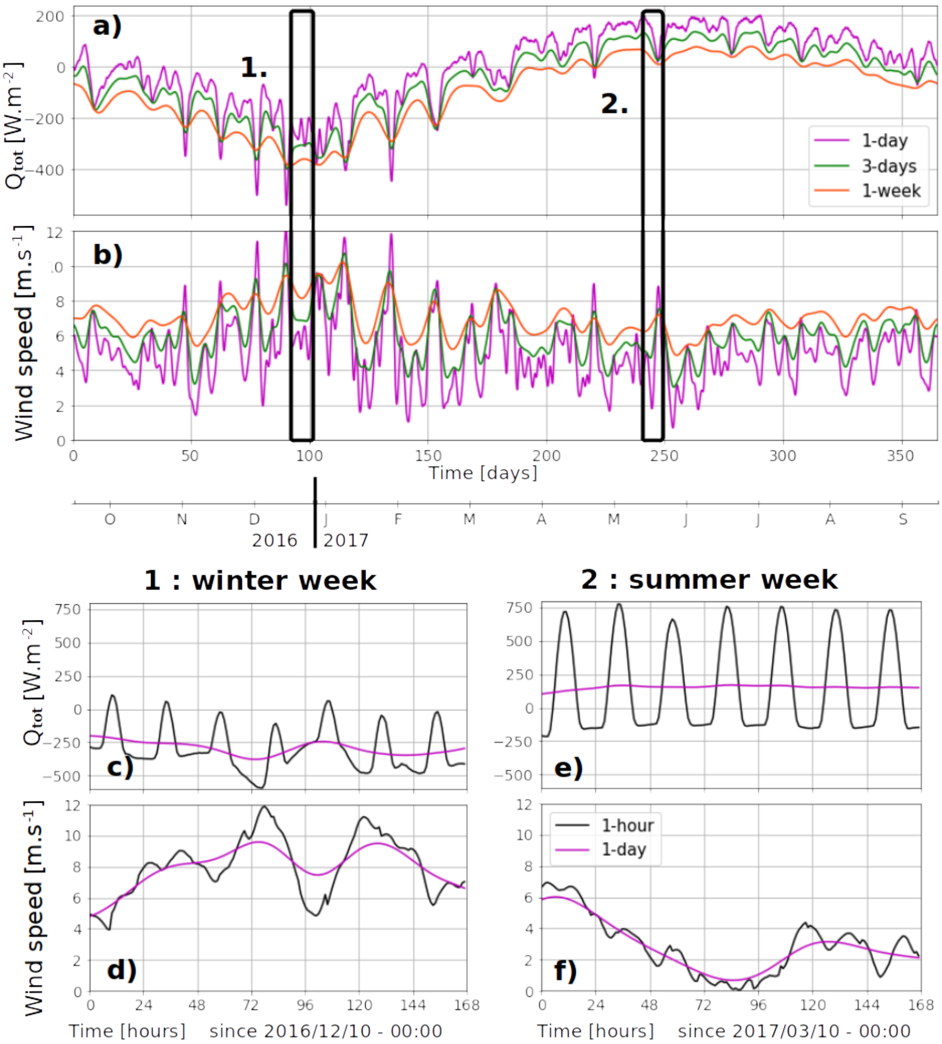

Figure 2. Net heat flux and wind speed from ERA5, for the 4 input time series, shown separately as diurnal cycle gives larger variations. (a) Net heat flux and (b) corrected wind speed (see Eq.12) for the 1-day (magenta line), 3-day (green) and 1-week (orange) time series over one year. To enhance readability, 3-day and 1-week net heat fluxes are lowered by 20 and 40 $W.m^{-2}$ respectively, and 3-day and 1-week wind speeds are heightened by 1 and $2 m.s^{-1}$ respectively. (c) 1-hour (black) and 1-day (magenta) net heat flux (respectively (d) for wind speed) in a winter week of 2016. (e) and (f) : same as (c) and (d) in a summer 2017 week.

To study the impact of temporal variability, four forcing inputs with different temporal scales are tested : 1-hour, 1-day, 3-day and 1-week. The 1-hour forcing is the original ERA5 time series, the three later ones are Gaussian smoothing of the 1-hour time series with window size (two standard deviations) of 1, 3 and 7 days respectively, shown in Fig.2. One year of forcing from 15 September 2016 to 15 September 2017 runs cyclically for 2 years as forcing input, with mean wind speed magnitude $V_{rms} = 5.0 m.s^{-1}$. 10m neutral wind from ERA5 is used for wind stress in Eq.11. To keep the same wind speed magnitude with varying wind frequency, smoothed time series for zonal and meridional winds ($[u]$ and $[v]$) have to be re-scaled. The correction factor λ being $\gtrsim 1.1$ for 1-day time series, and $1.1 < \lambda < 2$ for 3-day and 1-week :

$$\tilde{u} = \lambda[u]\,;\, \tilde{v} = \lambda[v] \quad \text{with} \quad \lambda = \frac{[\sqrt{u^2 + v^2}]}{\sqrt{[u]^2 + [v]^2}} \tag{12}$$

The same year is kept to avoid disturbance with interannual variations, which are strong for heat fluxes over the Mediterranean Sea (Mariotti, 2010; Pettenuzzo et al., 2010), but no significant variations were observed when selecting another year.

Forcing without surface temperature retroaction

A comparison experiment is run without SST retroaction on ocean-atmosphere fluxes. In this configuration, the net heat flux Q_{tot} from ERA5 directly forces the upper ocean layer, the short wave part $Q_{SW}(z)$ being still distributed on the vertical (Eq.8). Momentum fluxes are computed from Eq.11 with constant drag coefficient $C_D = 1.6 \times 10^{-3}$. The net heat flux Q_{tot} time series in ERA5 has daily amplitudes around $\pm 150 W.m^{-2}$ and an annual average of $-3.0\,W.m^{-2}$, consistent with the net evaporation of the Mediterranean Sea (Mariotti, 2010). Q_{tot} is then corrected by linearly decreasing the negative values to achieve a zero annual average, avoiding a drift of the mean stratification.

2.4 Eddy tracking indicators

Eddy shape, radius and intensity

Eddy detections are provided through the Angular Momentum Eddy Detection and Tracking Algorithm (AMEDA). AMEDA is a mixed velocity-altimetry approach, its relies on using primarily streamlines from a velocity field and identifying possible eddy centers computed as maxima of local normalized angular momentum (Le Vu et al., 2018). It was successfully used in several regions of the world ocean in altimetric data (Aroucha et al., 2020; Ayouche et al., 2021; Barboni et al., 2021), high frequency radar data (F. Liu et al., 2020) or numerical simulations (de Marez et al., 2021). In each eddy single observation (one eddy observed one day), AMEDA gives a center (which position is noted $\mathbf{X}_e$ hereafter), a maximal rotation speed V_{max} and two contours. The 'maximal speed' contour is the enclosed streamline with maximal speed (i.e. in the geostrophic approximation, with maximal SSH gradient) ; it is assumed to be the limit of the eddy core region where water parcels are trapped. The 'end' contour is the outermost closed SSH contour surrounding the eddy center and the maximal speed contour ; it is assumed to be the area of the eddy footprint, larger than just its core but still influenced by the eddy shear (Le Vu et al., 2018). The observed maximal speed radius R_{max} is defined as the radius of the circle having an area equal to the maximal speed contour. Eddy detection in real interpolated SSH observations leads to imperfections. It typically smooths gradients and then reduces observed geostrophic velocities (Amores et al., 2018; Stegner et al., 2021). To mimic those imperfections in the numerical simulations, AMEDA detections are performed on the 48h-averaged SSH field at model grid resolution, or interpolated at 2km if grid resolution is smaller.

Eddy SST signature δT, heat flux δQ, differential mixing ratio ξ and mixed layer anomaly

The anticyclone-induced SST signature δT is defined as the difference of SST between the eddy core SST_{in} and its periphery SST_{peri}. Adapting Moschos et al. (2022), SST_{in} is the average of the area centered on $\mathbf{X}_e(t)$ with radius $2/3R_{max}(t)$; SST_{peri} is the average on an annular area centered on $\mathbf{X}_e$ with radius between $2/3R_{max}(t)$ and $2R_{max}(t)$. Positive (negative) δT then indicates a warm-core (cold-core) signature. Similarly the induced signature on total net heat flux is defined as δQ, with positive δQ for increased warming at the eddy core. Thermal heat flux feedback (THFF) is then defined as the linear regression of δQ as a function of δT over the second year of simulation (from 365 to 730 days, see Sect.3.3).

Differential mixing between the eddy core and outside-eddy are measured through the index ξ. Temperature vertical diffusivity κ computed by $k-\epsilon$ mixing closure from instantaneous history record is spatially averaged in the eddy core (κ^{AE}) and outside-eddy (κ^{Out}). The eddy core region corresponds here to the area around the eddy center with radius $2/3R_{max}(t)$. The outside-eddy region is defined as the area outside any 'end' contours detected by the tracking algorithm. Diffusivity spanning several orders of magnitude, differential mixing ξ is then evaluated as a vertical average of the ratio of these two quantities, typically using a depth $h = 20m$ to focus on the upper layers stratified in summer :

$$\xi = \frac{1}{h}\int_{-h}^{surf} \frac{\kappa^{AE}}{\kappa^{Out}} dz \tag{13}$$

Summer eddy SST signature magnitude $\overline{\delta T}$ is defined as the 30th δT percentile over the summer, and its spread as the difference between the 30th and the 10th percentiles (see results in Table 1). Similarly $\overline{\xi}$ is defined as the median of the ξ distribution over the summer, and its spread as the difference between the median and the 30th percentile. First and second summers are defined as 230 to 340 days and 590 to 700 days respectively, corresponding to the May to August period when a significant number of warm-core anticyclones are observed (Moschos et al., 2022).

Last, the MLD anomaly ΔMLD is defined as the maximal difference reached between the MLD outside- and inside-eddy, with a 1-day Gaussian smoothing to remove peaks. In the following numerical experiments running for 2 years, the first winter is considered as a transient period not retained for analysis. ΔMLD is then computed only for the second winter, defined as 450 to 590 days, corresponding to the December to April period, when maximal MLD are reached in the Mediterranean Sea (Houpert et al., 2015).

3 Idealized simulations compared to observations

The temporal evolution of mesoscale eddies in the Levantine basin can be retrieved for several anticyclones where Argo floats remained trapped several months, as extensively studied in Barboni, Coadou-Chaventon, et al. (2023). A marked seasonal signal is detected in both SST and vertical structure. An example is shown in Fig.3 with a Ierapetra anticyclone, a strong recurrent anticyclonic structure formed each year in the lee of Crete island (Ioannou et al., 2020). In the example shown below, δT index has a marked oscillation between a winter warm core and summer cold core. The weekly smoothed signature can be measured to about $\delta T \approx +0.7°C$ in both winters 2016-2017 and 2017-2018, and about $-0.3°C$ in summer 2017 (about $-0.2°C$ in summer 2018). The vertical structure could also be measured thanks to large Argo deployments (Fig.3h) ; due to errors in the salinity sensors, density in 2018 is estimated from temperature applying a linear regression using 2017 data. One can also notice the seasonal variations of the anticyclone maximal speed, with two maxima in late winter. This is consistent with kinetic energy inverse cascade maximal peak from submesoscale to mesoscale in kinetic energy distributions (Zhai et al., 2008; Steinberg et al., 2022), but it is still noticeable to have the same phenomenon tracking a single individual structure. In this study the physical processes driving these observed seasonal variations are studied with numerical experiments, investigating sensitivity to horizontal and vertical resolutions, forcing frequency and SST retroaction on air-sea fluxes. Simulations are summarized in Table 1, the reference considered being 1km resolution with 1-hour forcing, 100 vertical levels with SST retroaction (run 1K100-1H in Table 1 below).

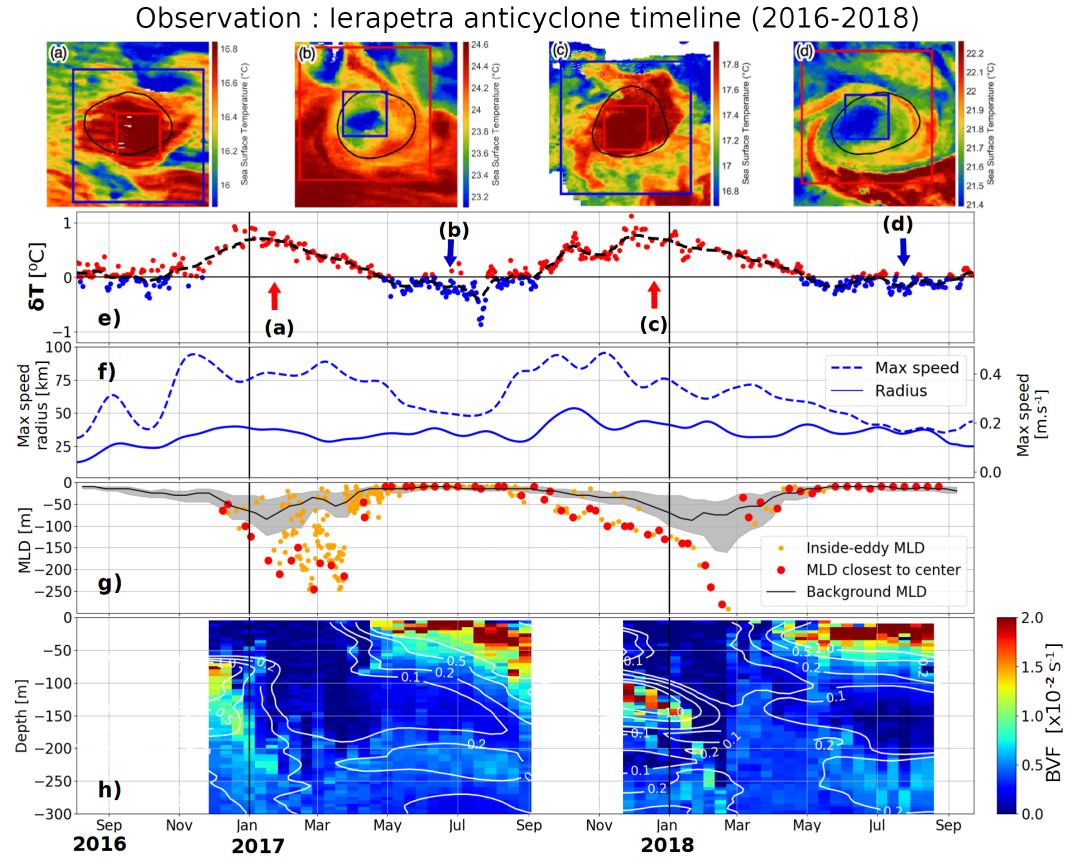

Figure 3. Temporal evolution of the Ierapetra anticyclone formed South-East of Crete in late summer 2016. Upper panels are high-resolution SST snapshots in (a) January 2017, (b) June 2017, (c) December 2017 and (d) July 2018, the maximal speed contour (see Sect.2.4) is in black line. (e) Eddy SST anomaly δT, cold-core in blue and warm-core in red, with black dashed line showing the 5 days smoothed evolution. (f) Maximal speed V_{max} (dashed blue) and radius R_{max} (continuous blue) with 10 days smoothing. (g) MLD evolution inside the the anticyclone (dots, with red ones highlighting the closest to center), with outside-eddy background MLD in continuous black line (spread as 20-80 percentiles interval shown in gray shades). (h) Brunt-Vaisala frequency (BVF) Hovmöller diagram, with selected 0.001, 0.002, 0.01 and 0.01 s^{-1} stratification contours (using slight 2D smoothing for the contours only).

Table 1. Summary table of CROCO numerical experiments. Runs start in September of the atmospheric forcing time series. Thermal heat flux feedback (THFF), eddy SST anomaly index $\overline{\delta T}$ and differential mixing ratio $\bar{\xi}$ are defined in Sect.2.4, and $\bar{\xi}$ is computed over the upper 20m. Subscripts ($\bar{\xi}_1$,$\bar{\xi}_2$) refers to first and second summers defined as 230 to 340 days and 590 to 700 days respectively. ΔMLD refers only to the second winter defined as 450 to 590 days (see shades in Fig.4d-h).

Name	**Vertical levels (minimal dz in meters)**	**dx** (km)	**Freq**	**SST retroaction**	**THFF** ($W.m^{-2}.K^{-1}$)	$\overline{\delta \mathbf{T}}_\mathbf{1}$ ($^{\circ}C$)	$\overline{\delta \mathbf{T}}_\mathbf{2}$ ($^{\circ}C$)	$\bar{\xi}_\mathbf{1}$	$\bar{\xi}_\mathbf{2}$	**ΔMLD** (m)
1K100-1H	100 (3.5)	1	1-hour	Yes	-41.5 ± 1.3	-0.20 ± 0.10	-0.18 ± 0.04	3.05 ± 0.70	2.81 ± 0.74	51
2K50-1H	50 (7)	2	1-hour	Yes	-40.7 ± 1.0	-0.12 ± 0.14	-0.11 ± 0.06	1.54 ± 0.31	1.34 ± 0.22	63
4K25-1H	25 (15)	4	1-hour	Yes	-34.3 ± 1.8	0.01 ± 0.14	0.02 ± 0.10	1.10 ± 0.12	1.00 ± 0.12	48
05K150-1H	150 (2.5)	0.5	1-hour	Yes	-42.2 ± 33.9	-0.16 ± 0.10	-0.19 ± 0.06	2.58 ± 0.58	2.71 ± 0.45	91
1K40-1H	40 (9)	1	1-hour	Yes	-44.4 ± 2.4	-0.00 ± 0.10	-0.04 ± 0.02	1.22 ± 0.15	1.46 ± 0.19	10
2K80-1H	80 (4.5)	2	1-hour	Yes	-44.2 ± 1.3	-0.18 ± 0.15	-0.13 ± 0.07	2.73 ± 0.72	2.95 ± 1.24	60
1K100-1D	100 (3.5)	1	1-day	Yes	-42.1 ± 0.8	-0.21 ± 0.20	-0.31 ± 0.06	2.99 ± 0.44	3.34 ± 1.23	57
1K100-3D	100 (3.5)	1	3-day	Yes	-44.7 ± 1.0	-0.12 ± 0.14	-0.09 ± 0.03	1.41 ± 0.28	0.99 ± 0.09	70
1K100-1W	100 (3.5)	1	1-week	Yes	-41.0 ± 0.4	-0.05 ± 0.05	-0.03 ± 0.01	1.25 ± 0.14	1.02 ± 0.01	94
1K100-1H-NoSST	100 (3.5)	1	1-hour	No	-	-0.41 ± 0.16	-0.51 ± 0.00	2.60 ± 0.46	2.47 ± 0.25	18

3.1 Horizontal and vertical resolution sensitivity

The numerical simulation at 4km resolution and 25 vertical levels (run 4K25-1H in Table 1) reveals several discrepancies with real observations. A horizontal resolution of 4km is close to operational oceanography models in the Mediterranean Sea (Juza et al., 2016). At the surface, despite seasonal variations of the eddy SST signatures (Fig.4a-c) and in the δT index (Fig.4f), summer 'inverse' signatures are not retrieved, with no cold-core anticyclone. An erosion of the eddy strength is also noticeable, with V_{max}decreasing from $0.4m.s^{-1}$ to $0.15m.s^{-1}$ in 2 years, while its radius remains constant ($\approx 25km$, Fig. 4e). At depth, the mixed layer anomaly is significant, on the order of 50m (Fig.4g). Some bursts of differential mixing are observed in late winter from December to March when mixed layer instabilities and restratification processes can occur, with ξ reaching a few times values higher than 2 (Fig. 4h). However no differential mixing is retrieved in summer. In the eddy interior, the winter MLD cooling forms a homogeneous layer between 100 and 150m (Fig. 4i). These winter waters formed by convection do not accurately reproduce the homogeneous subsurface anticyclone cores, separated by persistent density jump or sharp temperature gradient (see continuous stratified layer in Fig.3h around 200m depth or other examples in Fig.4-5 from Barboni, Coadou-Chaventon, et al. (2023)). The inability to reproduce this mesoscale subsurface lens is not surprising given the low vertical resolution, the vertical steps being on the order of $20m$ at $100m$ depth.

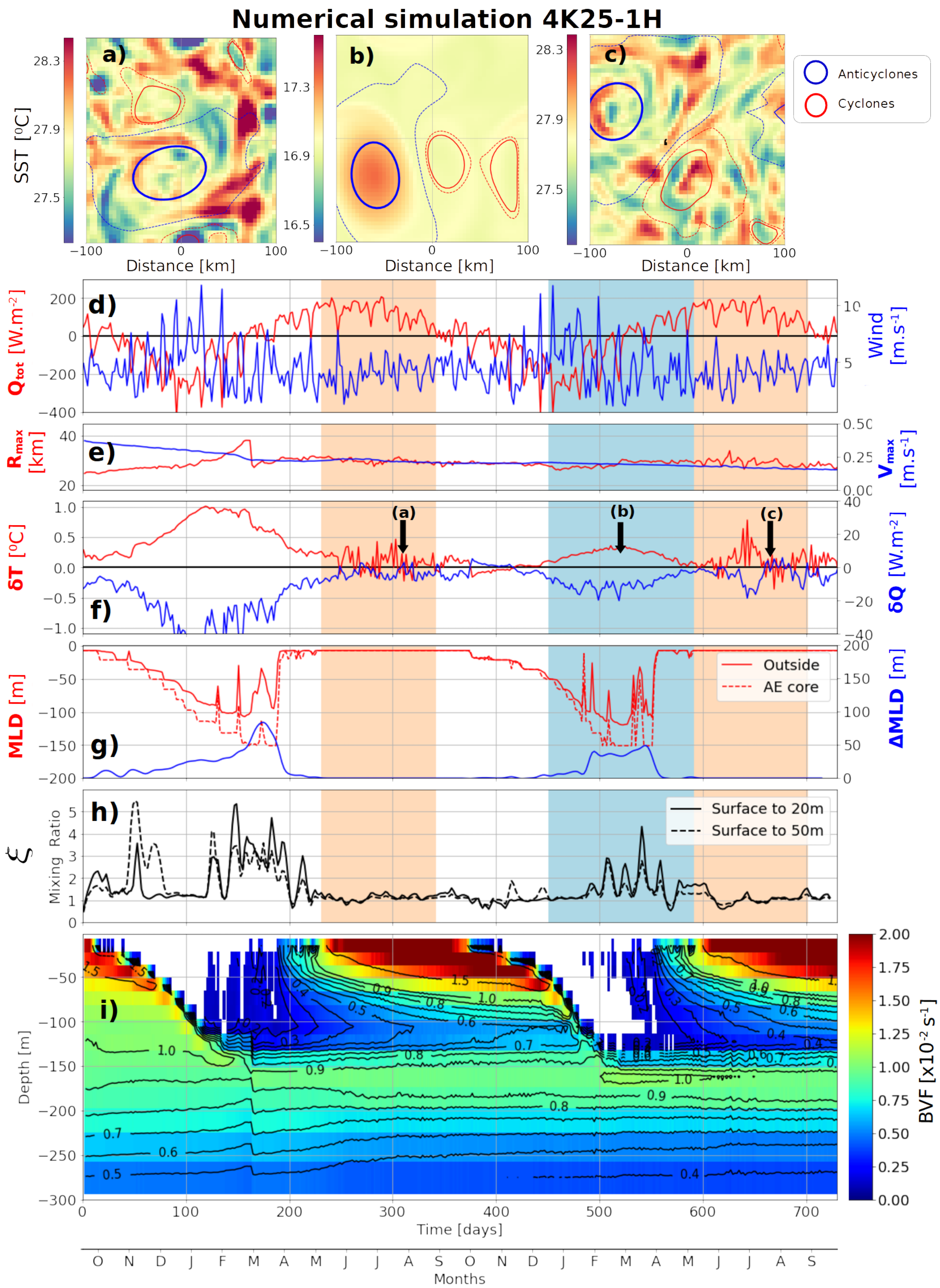

Figure 4. Simulation 4K25-1H from Table 1. (a) SST snapshot in the first summer, (b) in the second winter, (c) in the second summer, contours are AMEDA eddy detetions. The initial anticyclone is highlighted by a thicker line. (d) Net heat flux (red) and wind speed (blue). (e) R_{max} (red) and V_{max} (blue) from AMEDA. (f) SST anomaly index δT (red) and heat flux anomaly δQ (blue). (g) Mixed layer inside-eddy (dashed red) and outside-eddy (continuous red), mixed layer anomaly is in continuous blue. (h) Differential mixing ratio ξ defined in Eq.13 with $h = 20m$ (solid) and $h = 50m$ (dashed line). (i) Inside-eddy stratification evolution shown with Brunt-Vaisala frequency (scale factor 100) ; contours are overlaid with $0.001s^{-1}$ intervals and negative values are blanked. On panels d-h, summer periods are indicated by light red shades, winter by a light blue shade.

The same numerical set-up with a finer resolution (run 1K100-1H in Table 1) shows a net contrast with the previous coarser simulation. This simulation has a 1km horizontal grid size and 100 levels with same stretching parameters giving vertical grid steps close to 3m in the upper 200m. A summer 'inverse' eddy surface temperature is clearly retrieved with 1-hour frequency heat and momentum forcing. In this configuration, a clear anticyclonic cold-core SST signature is observed in summer (Fig.5a), switching back to a winter warm-core SST the next winter (Fig.5b) and appearing again in the second summer (Fig.5c). This anticyclone surface seasonal oscillation can clearly be tracked by δT (Fig.5f). $\overline{\delta T}$ reached about $-0.2°C$ in the both summers (see Table 1) with spikes of $\delta T \approx -0.5°C$ and maximal value around $+0.4°C$ in winter. Considering anticyclonic cold-core signatures statistics in the Mediterranean Sea (Moschos et al., 2022) in particular their Fig.5b) $\delta T \approx -0.2°C$ is a low but standard value, anticyclone SST anomalies typically not being colder than $-0.5°C$. This cold-core summer signature goes along with a mixing increase in the upper layers at the eddy core, measured by a diffusivity in summer more than twice stronger inside the eddy core than outside. Sensibility of the ξ indicator is shown on Fig.5h, with ξ averaged over the upper 20m or 50m, the first case leading to ξ values higher than 4 in summer despite some variability. This enhanced mixing seems to be confined in the upper layers, as ξ decreases to approximately 1 as soon as the mixed layer deepens, but it increases again to similar values during the second summer.

At depth, after the first transient winter, the maximal mixed layer anomaly reaches about 50m (Fig.5g), very close to the value of the simulation at 4km resolution. However the vertical structure is better reproduced at 1km, and in particular between 100 and 150m deep the $5{\times}10^{-3}s^{-1}$ stratification isoline closes in December, 4 months later than in the 4km simulation (in August, see Fig.4i). This means that homogeneous waters formed at depth in the first winter restratify more slowly. Eddy decay in time is also slower on maximal speed : after 2 years the anticyclone velocity is about $0.3m.s^{-1}$ with 1km resolution compared to $0.15m.s^{-1}$ with 4km (Fig.4e). Sharp density gradients are smoothed in a coarser simulation, leading to unrealistic temporal evolution of the anticyclones vertical structure. Surface (SST) or depth-integrated (maximal geostrophic speed) measurements are then not accurately reproduced at a spatial resolution of 4km.

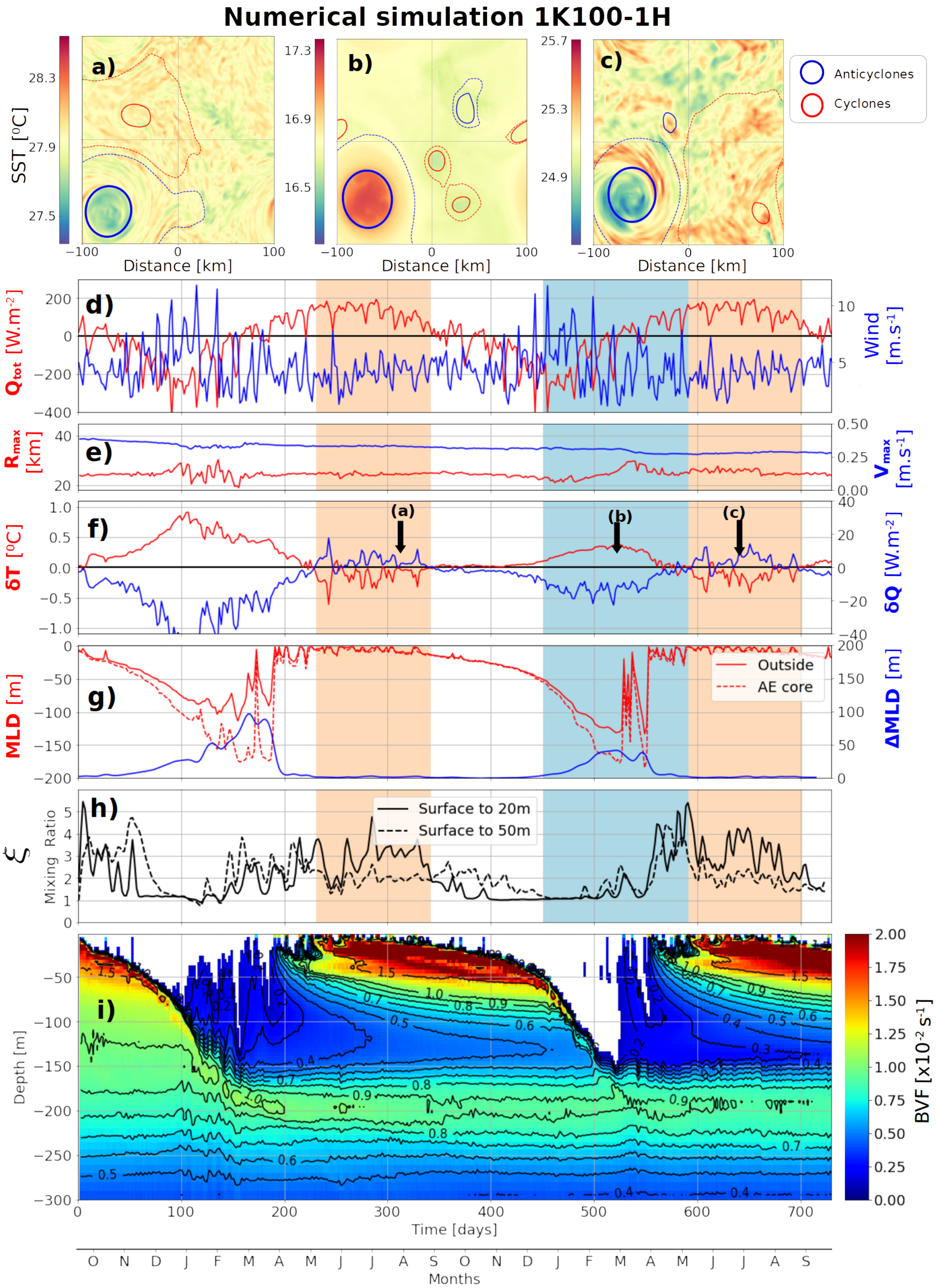

Figure 5. Simulation 1K100-1H from Table1. Same as in Fig.4 but with a 1km horizontal resolution.

An experimental series with the same numerical set-up is performed, increasing horizontal resolution from 4km to 500m and also vertical resolution, listed in Table 1. In runs 05K150-1H, 1K100-1H, 2K50-1H and 4K25-1H, horizontal to vertical resolutions ratio is kept similar to the ratio of Brunt-Vaisala frequency over Coriolis parameter, about

1000/3 (vertical grid step is then about 3m near surface in run 1K100-1H). In runs 2K80-1H horizontal resolution (2km) is coarser but vertical grid step smaller (about 4.5m in the upper layers), while in run 1K40-1H horizontal resolution (1km) is refined but vertical grid step larger (about 9m in the upper layers). Comparison of SST signatures and differential mixing (Fig.6c) reveals that summer anticyclonic cold-core signature $\overline{\delta T}$ and differential mixing $\overline{\xi}$ both continuously increase when decreasing the vertical grid cell. Summer eddy SST inversions are also consistently correlated with an increased mixing. In addition a convergence behavior is observed for more than 80 vertical levels to $\overline{\xi} \approx 3$, as no further mixing is obtained increasing the resolution to 150 levels. On the other hand very similar δT are retrieved in winter at all resolution, with a maximum around $+0.4°C$ (Fig.6a) and similar THFF suggesting that winter thermal loss is less affected by grid resolution. THFF slightly decreases for lower horizontal resolution, likely due to smoothing effect of strong SST patterns.

Significant differential mixing in run 2K80-1H with only 2km horizontal resolution but refined vertical grid implies that explicit resolution of vertical gradients are at stake, which is expected to resolve near-inertial waves. 2km horizontal resolution with a baroclinic first deformation radius around 11km entails that deformation radius is only partly resolved, as noticed in other numerical studies (Marchesiello et al., 2011; Soufflet et al., 2016). This further highlights the key role of vertical resolution in accurately resolving eddy SST anomalies.

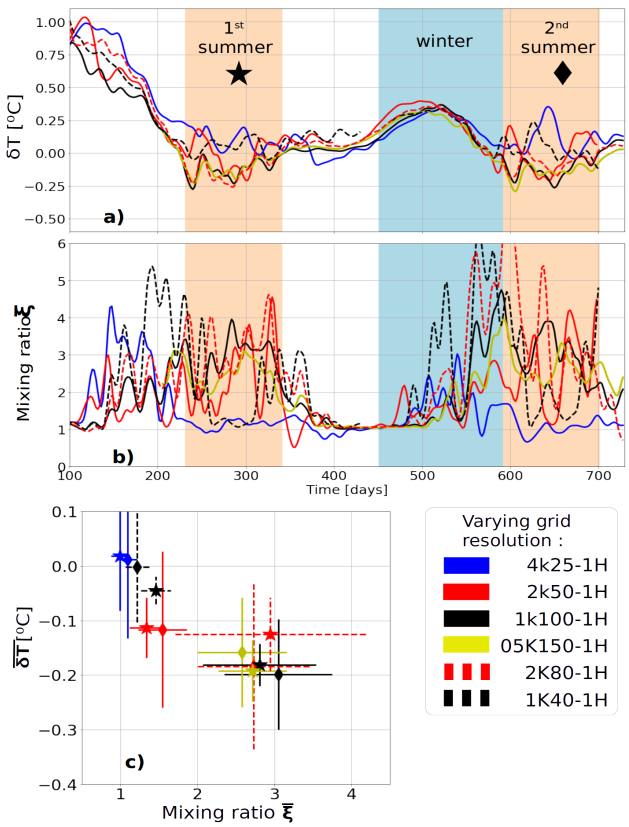

Figure 6. (a) δT and (b) ξ time series for experiments 1K100-1H, 2K50-1H, 4K25-1H, 05K150-1H listed in Table 1 with SST retroaction on air-sea fluxes and varying horizontal resolution frequency. 2-days Gaussian smoothing is applied and summer periods are shaded in light red, winter in light blue. Due to computer memory issues, the first transient winter at 500m resolution was not recorded. (c) Summer-averaged eddy-induced SST anomalies ($\overline{\delta T}$) and mixing ratio ($\overline{\xi}$), with stars for the first summer and diamonds for the second one. Errorbars are ξ spread (30^{th} percentile) over the same period.

For the eddy-induced mixed layer anomaly, similar values are obtained from 4km to 1km horizontal resolution ($\Delta MLD \approx 50m$), but a larger $\Delta MLD = 91m$ is retrieved at 500m resolution. This effect could be due to the partial resolution of sub-mesoscale processes such as mixed layer instabilities (Boccaletti et al., 2007; Capet et al., 2008). Maximal background mixed layer deepens when resolution gets finer down to 1km resolution (see Fig.4g and 5g), in consistence with previous experiments (Couvelard et al., 2015). At 500m resolution, a closer look at the MLD evolution inside- and outside-eddy shows that the outside-eddy MLD restratified earlier in run 05K150-1H (in March) than in run 1K100-1H (in April) due to restratification beginning at submesoscale with mixed layer instabilities (Fig.7b). But in both cases inside-eddy MLD reached the same depth (about $190m$, see Fig.7e-f). This suggests that maximal mixed layer inside-eddy indeed reached a maximum driven by air-sea cooling, while restratification outside-eddy occurred too late in run 1K100-1H because vertical buoyancy fluxes are too weak (Capet et al., 2008). Compared to Mediterranean MLD climatology, a restratification in April is indeed quite late (Houpert et al., 2015).

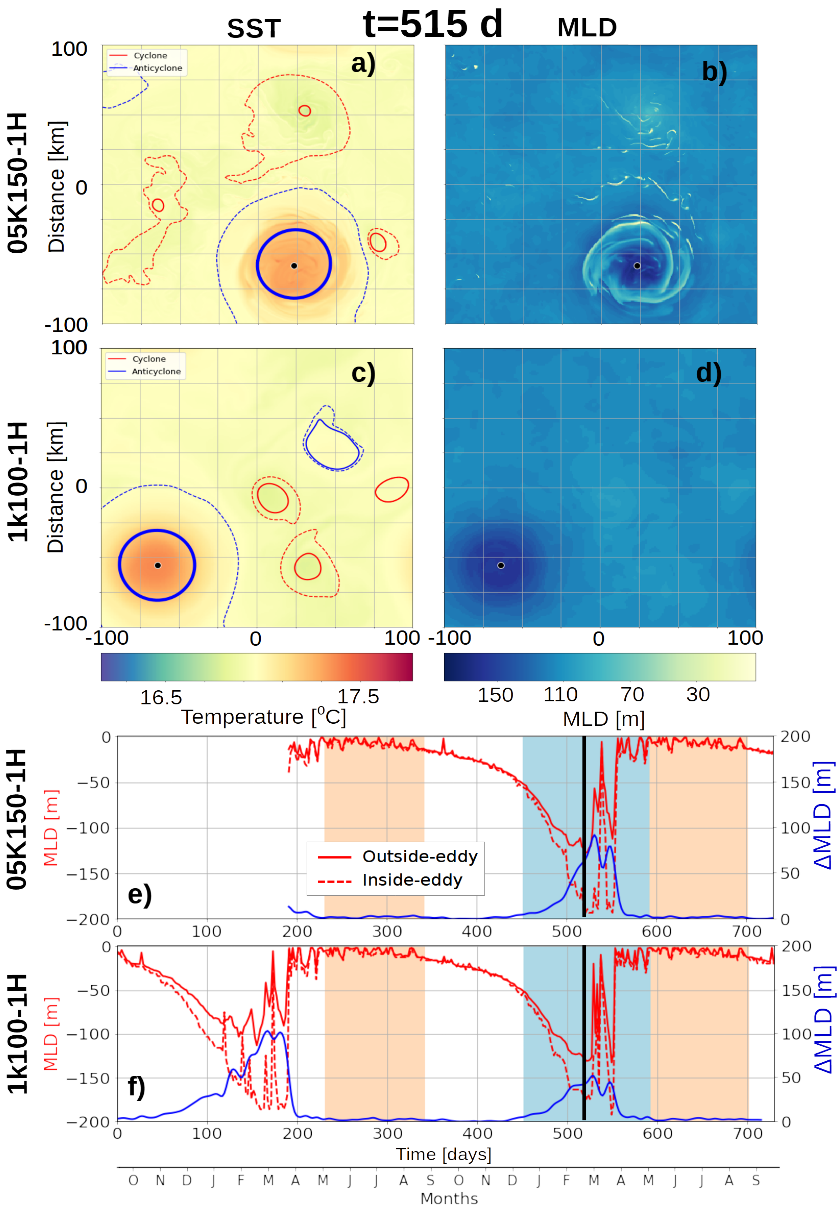

Figure 7. (a) SST with anticyclones and cyclones as in Fig.4 (the initial anticyclone has thicker contour) for the 05K150-1H simulation. (b) MLD in 05K150-1H. (c) and (d) : same as (a) and (b) but for the 1K100-1H simulation. (e) MLD time series inside-anticyclone (dashed red), outside-eddy (continous red) and ΔMLD (blue) for the 05K150-1H simulation, a black line indicates the time step shown in panels (a)-(d). Due to memory issues, the first transient winter was not recorded. (f) Same as (e) in 1K100-1H simulation.

Mixing patterns over the vertical in the high resolution simulations are also consistent with observations. Anticyclones were recently observed to enhance mixing at depth through the propagation of trapped near-inertial internal waves in their core. In studies from Martínez-Marrero et al. (2019) and Fernández-Castro et al. (2020), in situ measurements revealed lower dissipation rate ϵ in anticyclonic homogeneous core than in the neighboring background, and enhanced ϵ below at depth. In our numerical experiments, both diffusivity κ (Fig.8c) and dissipation rate ϵ (Fig.8e for run 1K100-1H) match this feature, with enhanced mixing in summer below the anticyclone, up to one order of magnitude larger from 200 to 300m depth. The anticyclone subsurface core revealed by thick isopycnal displacement on Fig.8e, also shows locally reduced ϵ between 100 and 200m. Fig.8e is then a striking reproduction of dissipation rate section obtained by Fernández-Castro et al. (2020) (see in particular their Fig.5f). However those in situ measurements could not compare outside- and inside-eddy mixing close to the surface, because the value range for ϵ would be too large with surface processes a lot more powerful than deep ocean ones. Numerical simulation enables to reveal that anticyclones also enhance mixing in near surface, with higher ϵ and κ just above the homogeneous core, in the upper 50 meters. The differential mixing ratio ξ previously shown in anticyclone time series then accurately measures a surface-enhanced mixing.

The seasonal cycle of eddy SST signature is then effectively reproduced at 1km horizontal resolution, close to observed value for the example shown above (Fig.3e). eddy SST seasonal shift correlates with increased mixing at the anticyclone core, in consistence with Moschos et al. (2022) hypothesis. This differential mixing is absent at low vertical resolution. But it appears through $k-\epsilon$ mixing parametrization and converges with a sufficiently high number of vertical levels, with vertical grid step smaller equal or smaller than 4m in near surface.

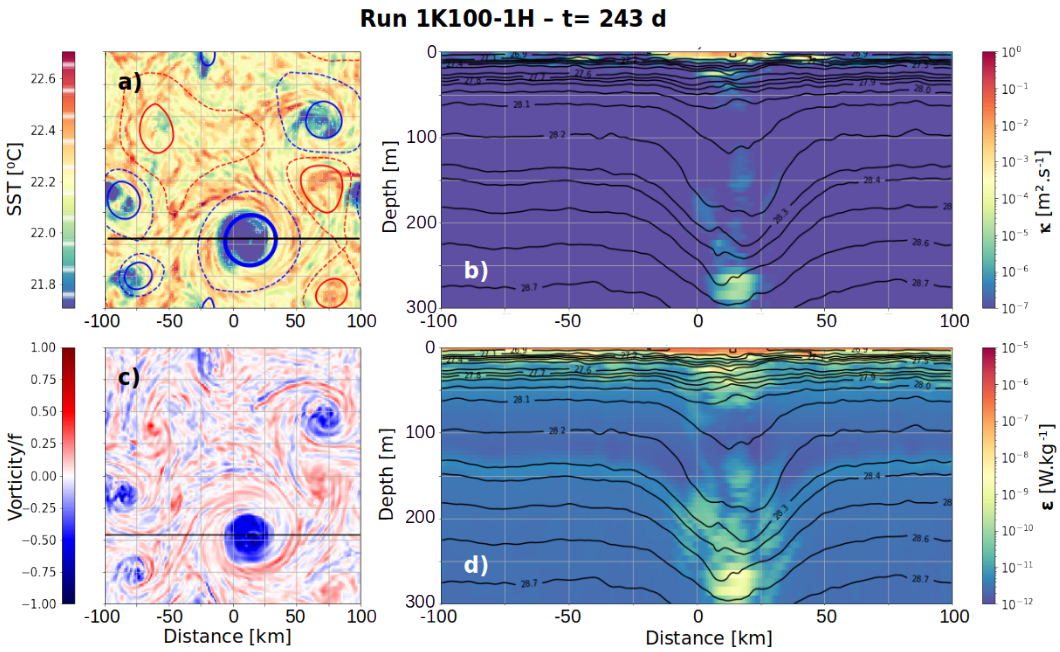

Figure 8. Snapshot at $t = 243\,d$ for the 1K100-1H simulation (see Fig.5). (a) SST and (c) surface vorticity normalized by f with eddy detections as in Fig.4 (initial anticyclone has a thicker contour). (b) κ and (d) ϵ vertical sections along black lines in panels (a)-(c) in the upper 300m with logarithmic color scales ; in both case the colorbar lower bound is the minimal possible value (see Sect.2.1). Isopycnals are added in black lines.

3.2 Forcing frequency sensitivity

Sensitivity of the eddy SST signature δT and differential mixing ξ to temporal resolution of the forcing is investigated by progressively removing high frequencies from the atmospheric inputs. These experiences are summarized as 1K100-1D to 1K100-1W in Table 1, using 1-day, 3-day and 1-week atmospheric time series respectively. δT and differential mixing ξ time series for these experiments are shown in Fig.9a-b. Significantly cold SST signatures ($\overline{\delta T} \lesssim -0.2°C$) are obtained together with strong mixing ratio ($\overline{\xi} \approx 3$) for 1-hour and 1-day frequency, but no significant differential mixing is retrieved ($1 < \overline{\xi} < 1.5$) for all lower forcing frequencies (Fig.9c). This threshold behavior is a strong result and shows that spontaneous appearance of differential mixing is driven by small scale and high frequency features. With a Coriolis parameter $f = 9.0 \times 10^{-5}s^{-1} = 1.24cpd$ (*count per day*), the inertial period is about 19h, the 1-day forcing can then partly trigger near-inertial waves.

The relationship between $\overline{\delta T}$ and $\overline{\xi}$ is however less clear than for the resolution sensitivity analysis (Fig.6). No differential mixing is observed for forcing frequencies lower than 1 day, but summer cold-core signatures are still found ($-0.12 < \overline{\delta T} < -0.03°C$, see Table1), even for the 1-week forcing. δT time series clearly show for all frequencies a marked seasonal signal (Fig.9a). In particular a significant warm winter signature is always observed, with stable maximal value at $\delta T \approx +0.4°C$. In the same context a surprising result is the summer averaged $\overline{\delta T}$ being colder on average at 1-day than 1-hour forcing, despite similar differential mixing. Temporal evolution of eddy SST anomalies reveals this effect to be caused by a larger oscillation of the eddy surface signature (Fig.9a) about $\pm 0.2°C$, hence larger errorbars at 1-day on Fig.9c. This suggests that other mechanisms not triggered by high frequency winds also contribute to the eddy SST seasonal cycle. If no differential vertical mixing is observed but if seasonal variations of the anticyclone SST (and hence surface density) is found, one can only hypothesize the role of lateral exchanges. Despite some tries, we were unsuccessful in quantifying eddy lateral exchanges following a varying $R_{max}(t)$ contour. No particular asymmetric wave modes was observed on SST snapshots, discarding the hypothesis of vortex Rossby waves (Guinn & Schubert, 1993; Montgomery & Kallenbach, 1997).

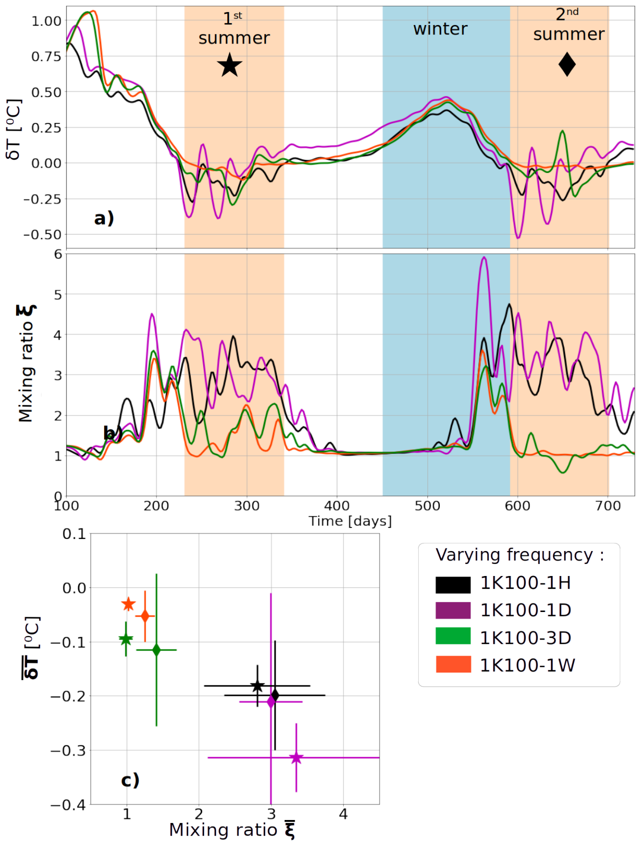

Figure 9. (a) δT and (b) ξ time series for experiments 1K100-1H, 1K100-1D, 1K100-3D and 1K100-1W listed in Table 1 with SST retroaction on air-sea fluxes and varying forcing frequency. Gaussian smoothing with 1-day standard deviation is applied, summer periods are shaded in light red, winter in light blue. (c) Summer-averaged eddy-induced SST anomalies ($\overline{\delta T}$) and mixing ratio ($\bar{\xi}$), with stars for the first summer and diamonds for the second one.

Near-inertial internal waves are investigated using Fourier transforms on vertical speed anomalies in run 1K100-1H. We focus on a single vertical level at 20m in near-surface where the enhanced mixing occurs (see Fig.8c). Transforms are computed only in the second summer (590 to 700 simulated days) with a 1-hour sampling frequency. Following Babiano et al. (1987), inside-eddy spectrum is performed keeping only the eddy core area (around the eddy center with radius $2/3R_{max}(t)$) and the remaining area is set to 0 before performing the Fourier transform. Similarly outside-eddy spectrum is performed blanking all value inside any eddy contours. The results clearly show a differential effect inside-eddy vertical kinetic energy density revealing a second powerful peak at the effective inertial frequency $f_e = f + \zeta/2 \approx 1.0cpd$, lower than the inertia frequency (Fig.10a). Outside-eddy spectrum (Fig.10b) shows only one peak at the inertial frequency, and internal waves cannot propagate at lower frequencies due to the f-cut-off (Garrett & Munk, 1972). Normalizing by the investigated area, total vertical kinetic energy per unit surface is indeed higher inside the anticyclone ($4.19{\times}10^{-14}m^2.s^{-2}/m^2$) than outside-eddy ($1.64{\times}10^{-14}m^2.s^{-2}/m^2$) due to these powerful sub-inertial internal waves. Further investigation confirmed that sub-inertial waves are absent inside-eddy with the 1-week forcing (Fig.13). An assumption of this method is however to assume that both inside- and outside-eddy areas roughly keep the same area, which is verified. This result is consistent with (Kunze, 1985) theory and recent numerical works (Danioux et al., 2015; Asselin & Young, 2020) sub-inertial waves ($\omega \lesssim f$) can be trapped in the anticyclone due to the locally lower absolute vorticity, and enhance mixing while breaking as proposed by Fernández-Castro et al. (2020).

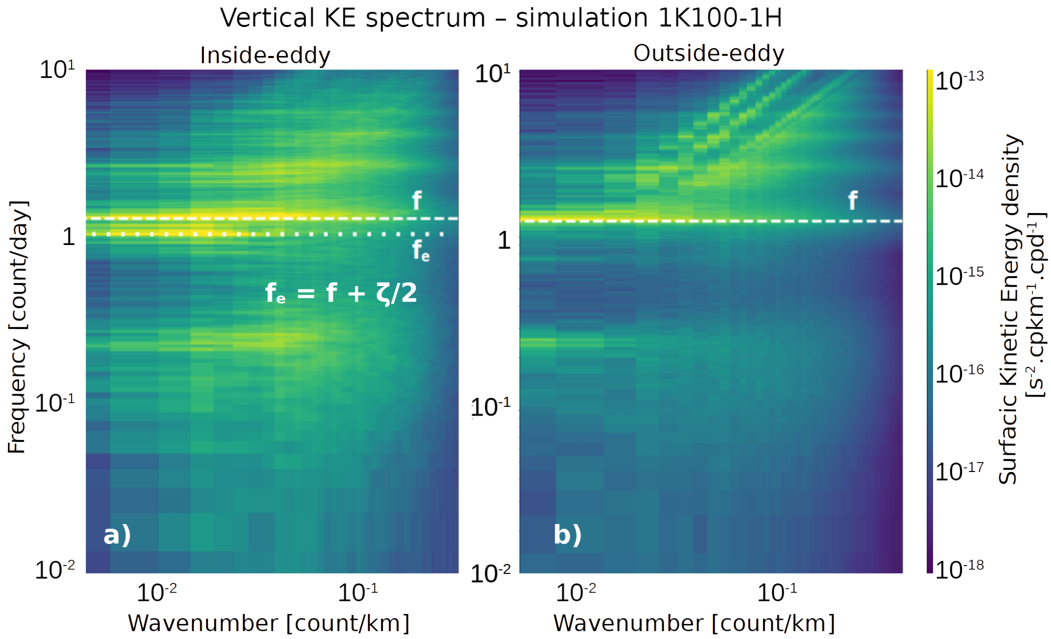

Figure 10. (a) Inside-eddy and (b) outside-eddy vertical kinetic energy density spectrum at 20m depth. For comparison, spectrum are normalized by the area of interest. Analysis performed on simulation 1K100-1H with 1-hour sampling. Normal (respectively effective) inertial frequencies $f = 1.24cpd$ ($f_e \approx 1.0cpd$) are highlighted by a white dashed (dotted) line.

3.3 Air-sea fluxes sensitivity

Sensitivity of the anticyclone temporal evolution to air-sea fluxes components is further investigated. A $1km$ resolution simulation experiment is run similarly as the 1K100-1H simulation without applying SST retroaction on air-sea fluxes (see Sect.2.3, run 1K100-1H-NoSST in Table 1). Although quite unrealistic, this experiment enables to check if the eddy SST anomaly seasonal shift and differential mixing observed in previous simulations are triggered by air-sea fluxes retroaction. Time series for SST reveals that eddy SST anomalies seasonal oscillation is retrieved without SST retroaction (Fig.11a-c), and summer cold-core signatures are even stronger : $\overline{deltaT} \approx -0.5°C$ for both summers (Fig.11f). Simultaneously, differential mixing reaches $\xi \approx 3$, approximately the same value as run 1K100-1H (Fig.11h). This confirms that differential eddy mixing triggering the eddy SST variations is not linked to air-sea fluxes retroaction. However this feedback can modulate and dampen the δT seasonal cycle leading to reduced anomalies.

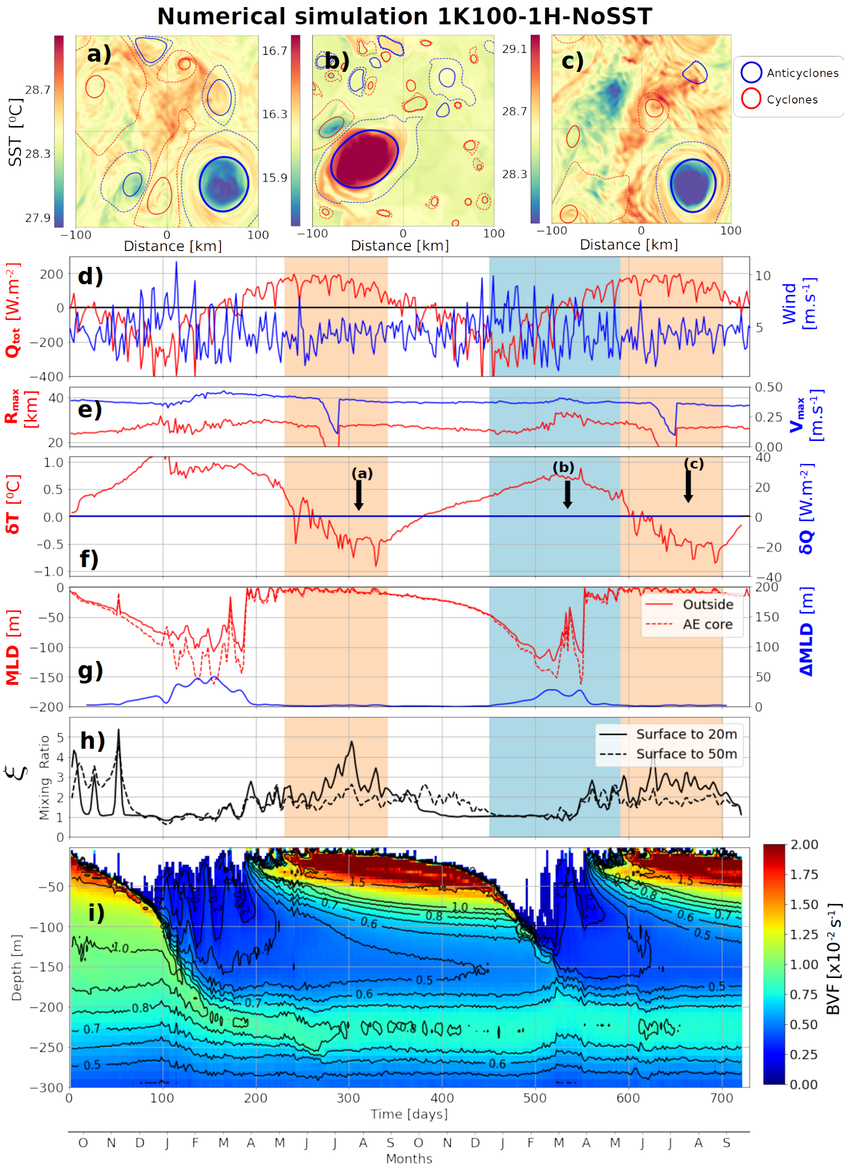

Figure 11. Simulation 1K100-1H-NoSST from Table 1. Same as in Fig.4 but without SST retroaction on air-sea fluxes. Discontinuities in R_{max} and V_{max} in panel (e) are due to the anti-cyclone crossing twice the grid borders.

SST retroaction acting as a negative feedback on SST anomalies can be analytically expected as linear. The derivative of each heat component with respect to T_s is indeed approximately constant (T_s being in Kelvin in Eq.14). Transfer coefficients C_E and C_S are indeed much more dependent on wind speed than on temperature, varying roughly about 0.2 with a T_s change of $1K$. The most sensitive case is a low air-sea temperature difference with weak wind, in which the boundary layer can switch from stable to unstable conditions (see for instance Fig.A1b from Pettenuzzo et al. (2010)). Assuming C_E and C_S are roughly constant with respect to temperature one gets :

$$\frac{\partial Q_{LW}^{\uparrow}}{\partial T_s} = -4\epsilon_{sb}\sigma_{sb}T_s^3 \approx -6\,W.m^{-2}.K^{-1} \tag{14}$$

$$\frac{\partial Q_{Lat}}{\partial T_s} \approx -\frac{\rho_a L_E C_E |V| 0.610}{P_{SL}} \frac{dP_{sat}}{dT_s} \approx -30\, W.m^{-2}.K^{-1} \tag{15}$$

$$\frac{\partial Q_{Sen}}{\partial T_s} = -\rho_a c_p C_S |V| \approx -10\, W.m^{-2}.K^{-1} \tag{16}$$

These estimations are in agreement with recent statistical observations from Aguedjou et al. (2023) who found contributions about $-25\, W.m^{-2}.K^{-1}$ and $-8\, W.m^{-2}.K^{-1}$ for latent and sensible heat fluxes respectively in the Tropical Atlantic Ocean. Altogether a thermal feedback on the order of $\frac{\partial Q_{tot}}{\partial T_s} \approx -45 W.m^{-2}.K^{-1}$ is then expected, mostly driven by latent heat flux. THFF in Table 1 is computed only on the whole simulated year (from 365 to 730 days) and a value of $\approx -40\, W.m^{-2}.K^{-1}$ is retrieved with a simple SST retroaction, in consistence with Eq.14 to 16. This value is relatively constant in our simulations, slightly decreasing for coarser resolution and lower forcing frequencies (see Table 1). $\partial C_E/\partial T_s$ and $\partial C_S/\partial T_s$ being also positive, taking this into account in Eq.15 would lead to a even higher THFF estimate. THFF for the 1K100-1H simulation, defined here as δQ as a function of δT is shown in Fig.12. The obtained thermal feedback is consistent with previous estimates in coupled climate model : Ma et al. (2016) found a higher THFF ranging between 40 and $56 W.m^{-2}.K^{-1}$ but in the specific area of very warm eddies of the Kuroshio extension region. Moreton et al. (2021) found THFF ranging between 35 and $45\, W.m^{-2}.K^{-1}$ over mesoscale eddies. They however used a composite approach in a model coupled with atmosphere and maximal oceanic resolution of $1/12°$, for effective radius about $40 km$. A coupled atmosphere layer is expected to further dampen the total THFF, taking into account other feedbacks than SST, in particular evaporation. Humidity is expected to increase over warm eddy, consequently decreasing the latent heat flux driving evaporation, whereas we applied a uniform h_{2m} field. Similar THFF in our simulations compared to coupled ocean-atmosphere models suggests that our results would not change significantly with more complex heat flux retroaction.

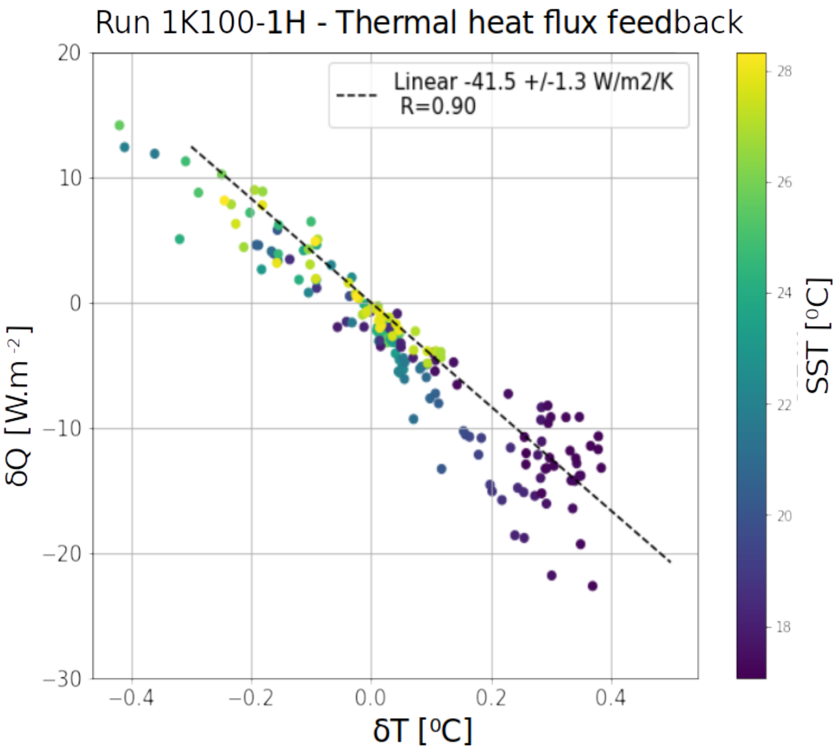

Figure 12. Thermal heat flux feedback in run 1K100-1H on the 2^{nd} simulated year, with linear regression as dashed black line, δQ and δT are from Fig.5f. Regression coefficient and parameters are indicated in the legend.

Without SST retroaction on air-sea fluxes, the most important difference from run 1K100-1H is the MLD anomaly variations. Outside-eddy, mixed layer evolution is very similar in runs 1K100-1H and 1K100-1H-NoSST reaching about $120m$ at its winter maximum, but the eddy MLD anomaly is about 5 times smaller ($\Delta MLD = 18m$, see Fig.11h). With no THFF, the MLD deepens at the same rate outside- and inside-eddy. Winter MLD deepening can be computed estimating the thermal loss ΔT, assuming a linear thermal linear stratification $\partial_z T$:

$$MLD = \frac{\Delta T}{\partial_z T} \tag{17}$$

The thermal loss is the integration of the heat flux over winter duration D. Assuming stratification is at first order the same outside- and inside-eddy, MLD anomaly would then be driven only by heat flux lateral gradients :

$$\Delta MLD = \frac{D}{\rho_0 c_p \partial_z T} \delta Q \tag{18}$$

In the 1K100-1H run with SST retroaction on air-sea fluxes, δQ is positive in winter reaching about $+15W.m^{-2}$ over 4 months. This leads to an estimate $\Delta MLD \approx 20m$. This is the estimated contribution on eddy MLD anomaly from THFF alone, but $\Delta MLD = 18m$ is still retrieved in run 1K100-1H-NoSST. It shows that difference between inside- and outside-eddy stratification also contribute to MLD anomaly in the absence of THFF. Assuming that $\partial_z T$ is roughly the same inside- and outside-eddy is valid in the upper layers where stratification is mostly the seasonal thermocline. At depth lower than 100m however, the anticyclone constitutes a more homogenized layer and this assumption should not hold. MLD is then expected to deepen faster inside-eddy even with no SST retroaction. An example in observations is shown in Fig.3g : the inside-eddy MLD connects in February 2018 with the layer homogenized the previous winter and reaching quickly about 300m. Such mixed layer deepening acceleration is partly retrieved in run 1K100-1H around 500 days, when the mixed layer reaches the subsurface homogenized layer formed in the first winter (Fig.5g). To sum up, ΔMLD is about 2 to 3 times smaller in run 1K100-1H-NoSST than in run 1K100-1H. This gives an estimate of the relative contribution of THFF and stratification difference on MLD anomalies.

In all simulations ΔMLD is anyway still relatively weak compared to the 200 to 300m MLD anomalies observed in Mediterranean anticyclones (Barboni, Coadou-Chaventon, et al., 2023). Two main hypotheses can be proposed, the first being that some interannual variability is needed. The second hypothesis is that layers homogenized by winter MLD progressively restratify at depth in summer due to numerical diffusion (stratification isolines progressively closing, Fig. 5i). MLD in the following winter will then have to break this artificial stratification. This second hypothesis entails that the vertical grid is not enough refined yet to correctly preserve homogenized layers from one winter to another. The comparison between runs 1K100-1H and 1K100-1H-NoSST shows that SST retroaction on air-sea fluxes is necessary to obtained eddy MLD anomalies, but quantitative description deserves further research and ΔMLD is not only driven by fluxes gradients at the eddy scale.

Conclusions

Idealized numerical experiments at high horizontal resolution and high frequency atmospheric forcing are able to qualitatively and quantitatively retrieve SST signature seasonal cycle for a mesoscale anticyclone. Starting from a surface intensified mesoscale anticyclone at $Ro \approx 0.16$, seasonal oscillations of the eddy SST anomalies are recovered with a 1km horizontal resolution, 100 vertical levels, hourly atmospheric forcing and SST retroaction on air-sea fluxes. Retrieved eddy anomalies are a warm winter SST feature at $\delta T \approx +0.5°C$ and a cold summer SST at $\delta T \approx -0.2°C$, in consistence with observations. The shift from warm winter SST signature to summer cold one is explained by an increased vertical mixing in the anticyclone upper layers. This differential mixing is due to higher NIW energy propagation well captured through the $\kappa - \epsilon$ mixing parametrization.

A sensitivity analysis reveals that this differential mixing depends on the grid vertical resolution. Model diffusivity near the surface is then consistently 3 times higher in summer inside-eddy than outside for vertical grid step about 4m or less in near surface. On the other hand horizontal resolution appears less critical to accurately resolve eddy differential mixing. Sensitivity to the forcing frequency is investigated by progressively removing high frequencies from the atmospheric input fields. A threshold behavior is observed when forcing frequency is lower than a day, then differential mixing dramatically vanishes with no significant summer cold-core anticyclonic SST. With high frequency forcing, vertical kinetic energy indeed reveals a second powerful peak only inside the anticyclone in near-surface, corresponding to internal waves at the effective inertial frequency. Such an analysis suggests a significant impact of the eddy vorticity as cut-off frequency in allowing or not the selective NIW propagation. Weaker eddy SST seasonal oscillations are also retrieved in the absence of high frequently forcing and consequently without differential mixing (3-day and 1-week experiments). This highlights that other contributions might participate to these eddy SST signatures, in particular lateral exchanges. A new question for future research opened by this eddy-modulated mixing is how it depends on the eddy vorticity and size.

SST retroaction on air-sea fluxes is not found to be responsible of eddy SST signatures seasonal shift, as the seasonal oscillation is retrieved with and without air-sea fluxes parametrization. However this retroaction is logically found to dampen the SST anomalies, and then reduces eddy anomalies magnitude in both summer and winter. The average thermal heat flux feedback of our mesoscale anticyclone is approximately $40 W.m^{-2}.K^{-1}$, in consistence with analytical derivation and previous studies.

Significant eddy-induced mixed layer anomaly $\Delta MLD \approx 50m$ are found at 1km horizontal resolution, only in the presence of SST retroaction on fluxes. Linear MLD anomaly analysis suggests that the thermal feedback is only responsible for about half of the MLD anomaly. Further analysis should then investigate how SST retroaction impacts inside-eddy stratification. MLD anomalies do not completely converge at 1km as larger anomalies are obtained with a 500m resolution due to restratification beginning outside-eddy driven by submesoscale instabilities, despite similar maximal mixed-layer at the anticyclone core. No restratification delay is clearly observed, but it could occur at even higher horizontal resolution inside the anticyclone because the balanced density gradients inhibits mixed layer instabilities there. This hypothesis is consistent with observations (Barboni, Coadou-Chaventon, et al., 2023) but would deserve more investigation in the future. This result is also important as the mixed layer is a significant driver of atmospheric and biogeochemical exchanges, and the explicit resolution of submesoscale processes might be needed to accurately reproduce their interaction with eddies (Capet et al., 2008; Lévy et al., 2018).

This is the first time that sub-inertial waves concentration in anticyclones is linked in a numerical study to an increased mixing in near surface, spontaneously retrieved through the $k-\epsilon$ mixing closure. Mixing modulation by eddies suggests a strong scale interactions between sub-inertial internal waves ($\omega \lesssim f$) and the mesoscale ($\omega \ll f$). Differential mixing triggered by high frequency winds is an important result highlighting the need of both fine vertical resolution and atmospheric forcing at sufficiently high frequency to correctly reproduce mesoscale eddies evolution. At present stage, global operational models do not have the resolution to capture these phenomena. According to this study vertical grid step about 4m in the upper thermocline would then be necessary to accurately reproduce mesoscale temporal evolution, or parameterize a differential mixing ratio $\xi \approx 3$ in near surface.

Open Research Section

In-situ profiles collocated ed with mesoscale eddies database is available at `https://doi.org/10.17882/93077`. AMEDA eddy tracking algorithm is open source and available at `https://github.com/briaclevu/AMEDA`. ERA5 atmospheric reanalysis are publicly available at `https://doi.org/10.24381/cds.adbb2d47`. The CROCO code is publicly available at `https://www.croco-ocean.org/`.

Acknowledgments
Authors gratefully acknowledge *Ifremer* and *Service Hydrographique et Océanographique de la Marine* for their use of the *Datarmor* computing facility. Authors acknowledge Evangelos Moschos (*Amphitrite*) for the reuse of his figures as snapshots in Fig.3a-d. Authors also acknowledge fruitful discussions with Clément Vic (*Ifremer*), in particular the comparison with observations in Fig.8 and 10, and the two anonymous reviewers whose comments greatly helped improving the present manuscript.

References

Aguedjou, H. M. A., Chaigneau, A., Dadou, I., Morel, Y., Baloïtcha, E., & Da-Allada, C. Y. (2023). Imprint of mesoscale eddies on air-sea interaction in the tropical atlantic ocean. *Remote Sensing*, *15*(12), 3087.

Amores, A., Jordà, G., Arsouze, T., & Le Sommer, J. (2018). Up to what extent can we characterize ocean eddies using present-day gridded altimetric products? *Journal of Geophysical Research: Oceans*, *123*(10), 7220–7236.

Arai, M., & Yamagata, T. (1994). Asymmetric evolution of eddies in rotating shallow water. *Chaos: An Interdisciplinary Journal of Nonlinear Science*, *4*(2), 163–175.

Aroucha, L. C., Veleda, D., Lopes, F. S., Tyaquiçã, P., Lefèvre, N., & Araujo, M. (2020). Intra- and inter-annual variability of north brazil current rings using angular momentum eddy detection and tracking algorithm: Observations from 1993 to 2016. *Journal of Geophysical Research: Oceans*, *125*(12), e2019JC015921. doi: 10.1029/2019JC015921

Asselin, O., & Young, W. R. (2020). Penetration of wind-generated near-inertial waves into a turbulent ocean. *Journal of Physical Oceanography*, *50*(6), 1699–1716.

Ayouche, A., De Marez, C., Morvan, M., L'hegaret, P., Carton, X., Le Vu, B., & Stegner, A. (2021). Structure and dynamics of the ras al hadd oceanic dipole in the arabian sea. In *Oceans* (Vol. 2, pp. 105–125).

Babiano, A., Basdevant, C., Legras, B., & Sadourny, R. (1987). Vorticity and passive-scalar dynamics in two-dimensional turbulence. *Journal of Fluid Mechanics*, *183*, 379–397.

Barboni, A., Coadou-Chaventon, S., Stegner, A., Le Vu, B., & Dumas, F. (2023). How subsurface and double-core anticyclones intensify the winter mixed-layer deepening in the mediterranean sea. *Ocean Science*, *19*(2), 229–250.

Barboni, A., Lazar, A., Stegner, A., & Moschos, E. (2021). Lagrangian eddy tracking reveals the eratosthenes anticyclonic attractor in the eastern levantine basin. *Ocean Science*, *17*(5), 1231–1250.

Barboni, A., Stegner, A., Le Vu, B., & Dumas, F. (2023). *2000-2021 in situ profiles colocalized with ameda eddy detections from 1/8 aviso altimetry in the mediterranean sea.* SEANOE.

Boccaletti, G., Ferrari, R., & Fox-Kemper, B. (2007). Mixed layer instabilities and restratification. *Journal of Physical Oceanography*, *37*(9), 2228–2250.

Capet, X., Mcwilliams, J. C., Molemaker, M. J., & Shchepetkin, A. F. (2008). Mesoscale to submesoscale transition in the california current system. part i: Flow structure, eddy flux, and observational tests. *Journal of physical oceanography*, *38*(1), 29–43.

Carton, X., Flierl, G., & Polvani, L. (1989). The generation of tripoles from unstable axisymmetric isolated vortex structures. *EPL (Europhysics Letters)*, *9*(4), 339.

Chaigneau, A., Eldin, G., & Dewitte, B. (2009). Eddy activity in the four major upwelling systems from satellite altimetry (1992–2007). *Progress in Oceanography*, *83*(1-4), 117–123.

Chelton, D. B., Gaube, P., Schlax, M. G., Early, J. J., & Samelson, R. M. (2011). The influence of nonlinear mesoscale eddies on near-surface oceanic chlorophyll. *Science*, *334*(6054), 328–332.

Chelton, D. B., Schlax, M. G., & Samelson, R. M. (2011). Global observations of nonlinear mesoscale eddies. *Progress in oceanography*, *91*(2), 167–216.

Couvelard, X., Dumas, F., Garnier, V., Ponte, A., Talandier, C., & Treguier, A.-M. (2015). Mixed layer formation and restratification in presence of mesoscale and submesoscale turbulence. *Ocean Modelling*, *96*, 243–253.

Danioux, E., Klein, P., & Rivière, P. (2008). Propagation of wind energy into the deep ocean through a fully turbulent mesoscale eddy field. *Journal of Physical Oceanography*, *38*(10), 2224–2241.

Danioux, E., Vanneste, J., & Bühler, O. (2015). On the concentration of near-inertial waves in anticyclones. *Journal of Fluid Mechanics*, *773*, R2.

D'Asaro, E. A. (1995). Upper-ocean inertial currents forced by a strong storm. part iii: Interaction of inertial currents and mesoscale eddies. *Journal of physical oceanography*, *25*(11), 2953–2958.

de Marez, C., Le Corre, M., & Gula, J. (2021). The influence of merger and convection on an anticyclonic eddy trapped in a bowl. *Ocean Modelling*, *167*, 101874.

Doglioli, A., Blanke, B., Speich, S., & Lapeyre, G. (2007). Tracking coherent structures in a regional ocean model with wavelet analysis: Application to cape basin eddies. *Journal of Geophysical Research: Oceans*, *112*(C5).

Escudier, R., Renault, L., Pascual, A., Brasseur, P., Chelton, D., & Beuvier, J. (2016). Eddy properties in the western mediterranean sea from satellite altimetry and a numerical simulation. *Journal of Geophysical Research: Oceans*, *121*(6), 3990–4006.

Everett, J., Baird, M., Oke, P., & Suthers, I. (2012). An avenue of eddies: Quantifying the biophysical properties of mesoscale eddies in the tasman sea. *Geophysical Research Letters*, *39*(16).

Fairall, C. W., Bradley, E. F., Hare, J., Grachev, A. A., & Edson, J. B. (2003). Bulk parameterization of air–sea fluxes: Updates and verification for the coare algorithm. *Journal of climate*, *16*(4), 571–591.

Fernández-Castro, B., Evans, D. G., Frajka-Williams, E., Vic, C., & Naveira-Garabato, A. C. (2020). Breaking of internal waves and turbulent dissipation in an anticyclonic mode water eddy. *Journal of Physical Oceanography*, *50*(7), 1893–1914.

Frenger, I., Gruber, N., Knutti, R., & Münnich, M. (2013). Imprint of southern ocean eddies on winds, clouds and rainfall. *Nature geoscience*, *6*(8), 608–612.

Garrett, C., & Munk, W. (1972). Space-time scales of internal waves. *Geophysical Fluid Dynamics*, *3*(3), 225–264.

Gaube, P., J. McGillicuddy Jr, D., & Moulin, A. J. (2019). Mesoscale eddies modulate mixed layer depth globally. *Geophysical Research Letters*, *46*(3), 1505–1512.

Graves, L. P., McWilliams, J. C., & Montgomery, M. T. (2006). Vortex evolution due to straining: A mechanism for dominance of strong, interior anticyclones. *Geophysical and Astrophysical Fluid Dynamics*, *100*(3), 151–183.

Guinn, T. A., & Schubert, W. H. (1993). Hurricane spiral bands. *Journal of the atmospheric sciences*, *50*(20), 3380–3403.

Hausmann, U., & Czaja, A. (2012). The observed signature of mesoscale eddies in sea surface temperature and the associated heat transport. *Deep Sea Research Part I: Oceanographic Research Papers*, *70*, 60–72.

Hersbach, H., Bell, B., Berrisford, P., Hirahara, S., Horányi, A., Muñoz-Sabater, J., ... others (2020). The era5 global reanalysis. *Quarterly Journal of the Royal Meteorological Society*, *146*(730), 1999–2049.

Houpert, L., Testor, P., De Madron, X. D., Somot, S., D'ortenzio, F., Estournel, C., & Lavigne, H. (2015). Seasonal cycle of the mixed layer, the seasonal thermocline and the upper-ocean heat storage rate in the mediterranean sea derived from observations. *Progress in Oceanography*, *132*, 333–352.

Ioannou, A., Stegner, A., Dubos, T., Le Vu, B., & Speich, S. (2020). Generation and intensification of mesoscale anticyclones by orographic wind jets: The case of ierapetra eddies forced by the etesians. *Journal of Geophysical Research: Oceans*, *125*(8), e2019JC015810.

Ioannou, A., Stegner, A., & Dumas, F. (2021). Three-dimensional evolution of mesoscale anticyclones in the lee of crete. *Frontiers in Marine Science*.

Ioannou, A., Stegner, A., Tuel, A., LeVu, B., Dumas, F., & Speich, S. (2019). Cyclostrophic corrections of aviso/duacs surface velocities and its application to mesoscale eddies in the mediterranean sea. *Journal of Geophysical Research: Oceans*, *124*(12), 8913–8932.

Juza, M., Mourre, B., Renault, L., Gómara, S., Sebastián, K., Lora, S., … others (2016). Socib operational ocean forecasting system and multi-platform validation in the western mediterranean sea. *Journal of Operational Oceanography*, *9*(sup1), s155–s166.

Kunze, E. (1985). Near-inertial wave propagation in geostrophic shear. *Journal of Physical Oceanography*, *15*(5), 544–565.

Laxenaire, R., Speich, S., Blanke, B., Chaigneau, A., Pegliasco, C., & Stegner, A. (2018). Anticyclonic eddies connecting the western boundaries of indian and atlantic oceans. *Journal of Geophysical Research: Oceans*, *123*(11), 7651–7677.

Laxenaire, R., Speich, S., & Stegner, A. (2020). Agulhas ring heat content and transport in the south atlantic estimated by combining satellite altimetry and argo profiling floats data. *Journal of Geophysical Research: Oceans*, *125*(9), e2019JC015511.

Le Vu, B., Stegner, A., & Arsouze, T. (2018). Angular momentum eddy detection and tracking algorithm (ameda) and its application to coastal eddy formation. *Journal of Atmospheric and Oceanic Technology*, *35*(4), 739–762.

Lévy, M., Franks, P. J., & Smith, K. S. (2018). The role of submesoscale currents in structuring marine ecosystems. *Nature communications*, *9*(1), 4758.

Liu, F., Zhou, H., Huang, W., & Wen, B. (2020). Submesoscale eddies observation using high-frequency radars: A case study in the northern south china sea. *IEEE Journal of Oceanic Engineering*, *46*(2), 624–633.

Liu, Y., Zheng, Q., & Li, X. (2021). Characteristics of global ocean abnormal mesoscale eddies derived from the fusion of sea surface height and temperature data by deep learning. *Geophysical Research Letters*, *48*(17), e2021GL094772.

Ma, X., Jing, Z., Chang, P., Liu, X., Montuoro, R., Small, R. J., … others (2016). Western boundary currents regulated by interaction between ocean eddies and the atmosphere. *Nature*, *535*(7613), 533–537.

Marchesiello, P., Capet, X., Menkes, C., & Kennan, S. C. (2011). Submesoscale dynamics in tropical instability waves. *Ocean Modelling*, *39*(1-2), 31–46.

Mariotti, A. (2010). Recent changes in the mediterranean water cycle: a pathway toward long-term regional hydroclimatic change? *Journal of Climate*, *23*(6), 1513–1525.

Martínez-Marrero, A., Barceló-Llull, B., Pallàs-Sanz, E., Aguiar-González, B., Gordo, C., Grisolía, D., … Arístegui, J. (2019). Near-inertial wave trapping near the base of an anticyclonic mesoscale eddy under normal atmospheric conditions. *Journal of Geophysical Research: Oceans*, *124*(11), 8455–8467.

Mason, E., Pascual, A., & McWilliams, J. C. (2014). A new sea surface height–based code for oceanic mesoscale eddy tracking. *Journal of Atmospheric and Oceanic Technology*, *31*(5), 1181–1188.

Mason, E., Ruiz, S., Bourdalle-Badie, R., Reffray, G., García-Sotillo, M., & Pascual, A. (2019). New insight into 3-d mesoscale eddy properties from cmems operational models in the western mediterranean. *Ocean Science*, *15*(4), 1111–1131.

Montgomery, M. T., & Kallenbach, R. J. (1997). A theory for vortex rossby-waves and its application to spiral bands and intensity changes in hurricanes. *Quarterly Journal of the Royal Meteorological Society*, *123*(538), 435–465.

Moreton, S., Ferreira, D., Roberts, M., & Hewitt, H. (2021). Air-sea turbulent heat flux feedback over mesoscale eddies. *Geophysical Research Letters*, *48*(20), e2021GL095407.

Moschos, E., Barboni, A., & Stegner, A. (2022). Why do inverse eddy surface temperature anomalies emerge? the case of the mediterranean sea. *Remote Sensing*, *14*(15), 3807.

Nencioli, F., Dong, C., Dickey, T., Washburn, L., & McWilliams, J. C. (2010). A vector geometry–based eddy detection algorithm and its application to a high-resolution numerical model product and high-frequency radar surface velocities in the southern california bight. *Journal of atmospheric and oceanic technology*, *27*(3), 564–579.

Paulson, C. A., & Simpson, J. J. (1977). Irradiance measurements in the upper ocean. *Journal of Physical Oceanography*, *7*(6), 952–956.

Penven, P., Halo, I., Pous, S., & Marié, L. (2014). Cyclogeostrophic balance in the mozambique channel. *Journal of Geophysical Research: Oceans*, *119*(2), 1054–1067.

Perfect, B., Kumar, N., & Riley, J. (2020). Energetics of seamount wakes. part i: Energy exchange. *Journal of Physical Oceanography*, *50*(5), 1365–1382.

Perret, G., Stegner, A., Farge, M., & Pichon, T. (2006). Cyclone-anticyclone asymmetry of large-scale wakes in the laboratory. *Physics of Fluids*, *18*(3).

Pessini, F., Olita, A., Cotroneo, Y., & Perilli, A. (2018). Mesoscale eddies in the algerian basin: do they differ as a function of their formation site? *Ocean Science*, *14*(4), 669–688.

Pettenuzzo, D., Large, W., & Pinardi, N. (2010). On the corrections of era-40 surface flux products consistent with the mediterranean heat and water budgets and the connection between basin surface total heat flux and nao. *Journal of Geophysical Research: Oceans*, *115*(C6).

Rodi, W. (1987). Examples of calculation methods for flow and mixing in stratified fluids. *Journal of Geophysical Research: Oceans*, *92*(C5), 5305–5328. doi: 10.1029/JC092iC05p05305

Shchepetkin, A. F., & McWilliams, J. C. (2005). The regional oceanic modeling system (roms): a split-explicit, free-surface, topography-following-coordinate oceanic model. *Ocean modelling*, *9*(4), 347–404.

Smith, W. H., & Sandwell, D. T. (1997). Global sea floor topography from satellite altimetry and ship depth soundings. *Science*, *277*(5334), 1956–1962.

Soufflet, Y., Marchesiello, P., Lemarié, F., Jouanno, J., Capet, X., Debreu, L., & Benshila, R. (2016). On effective resolution in ocean models. *Ocean Modelling*, *98*, 36–50.

Stegner, A., & Dritschel, D. (2000). A numerical investigation of the stability of isolated shallow water vortices. *Journal of Physical Oceanography*, *30*(10), 2562–2573.

Stegner, A., Le Vu, B., Dumas, F., Ghannami, M. A., Nicolle, A., Durand, C., & Faugere, Y. (2021). Cyclone-anticyclone asymmetry of eddy detection on gridded altimetry product in the mediterranean sea. *Journal of Geophysical Research: Oceans*, *126*(9), e2021JC017475.

Steinberg, J. M., Cole, S. T., Drushka, K., & Abernathey, R. P. (2022). Seasonality of the mesoscale inverse cascade as inferred from global scale-dependent eddy energy observations. *Journal of Physical Oceanography*, *52*(8), 1677–1691.

Sun, W., Dong, C., Tan, W., & He, Y. (2019). Statistical characteristics of cyclonic warm-core eddies and anticyclonic cold-core eddies in the north pacific based on remote sensing data. *Remote Sensing*, *11*(2), 208.

Sun, W., Dong, C., Wang, R., Liu, Y., & Yu, K. (2017). Vertical structure anomalies of oceanic eddies in the kuroshio extension region. *Journal of Geophysical Research: Oceans*, *122*(2), 1476–1496.

Sverdrup, H. U., Johnson, M. W., Fleming, R. H., et al. (1942). *The oceans: Their physics, chemistry, and general biology* (Vol. 1087) (No. 8). Prentice-Hall New York.

Trott, C. B., Subrahmanyam, B., Chaigneau, A., & Roman-Stork, H. L. (2019). Eddy-induced temperature and salinity variability in the arabian sea. *Geophysical Research Letters*, *46*(5), 2734–2742.

Umlauf, L., & Burchard, H. (2003). A generic length-scale equation for geophysical turbulence models. *Journal of Marine Research*, *61*(2), 235–265.

Villas Bôas, A., Sato, O., Chaigneau, A., & Castelão, G. (2015). The signature of mesoscale eddies on the air-sea turbulent heat fluxes in the south atlantic

ocean. *Geophysical Research Letters*, *42*(6), 1856–1862.
Zhai, X., Greatbatch, R. J., & Kohlmann, J.-D. (2008). On the seasonal variability of eddy kinetic energy in the gulf stream region. *Geophysical Research Letters*, *35*(24).

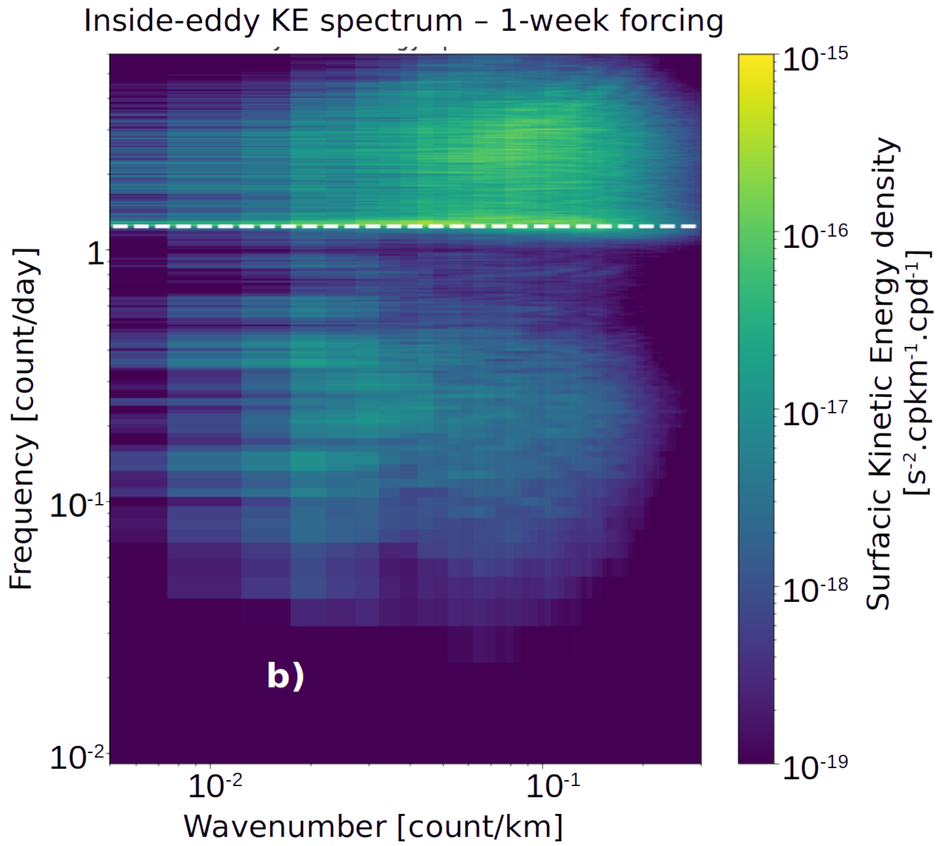

Figure 13. Inside-eddy vertical kinetic energy density spectrum at 20m depth in run 1K100-1W. For computational cost constraints, sampling is performed every 2 hours, then y-axis is slightly changed compared to Fig.10a, and colorbar is adapted. White dashed line shows inertial frequency.